Trees, Forests and People 26 (2026) 101326

Contents lists available at ScienceDirect

Trees, Forests and People

journal homepage: www.sciencedirect.com/journal/trees-forests-and-people

Multi-decadal assessment of climatic, productivity, and anthropogenic drivers of mangrove disturbance

Abdul Qaiyum Alidin [a,c], Azlizam Aziz [a], Waseem Razzaq Khan [b], Shazali Johari [a,c,*]

[a] Department of Recreation and Ecotourism, Faculty of Forestry and Environment, Universiti Putra Malaysia, Serdang, Selangor, Malaysia
[b] Department of Forestry Science and Biodiversity, Faculty of Forestry and Environment, Universiti Putra Malaysia UPM, Serdang 43400 Selangor, Malaysia
[c] i-CATS University College Jalan Stampin Timur 93350 Kuching, Sarawak, Malaysia

ARTICLE INFO

Keywords:
Mangrove disturbance
Climate anomalies
LandTrendr
Productivity anomalies
Remote sensing

ABSTRACT

Mangrove forests provide critical ecosystem services, yet global declines have accelerated under combined anthropogenic pressure and climate variability. Identifying which environmental and accessibility gradients are most strongly associated with canopy disturbance is important for monitoring and management. Here, multi-decadal Landsat time series (1990–2023) were analysed to map mangrove disturbance in Sarawak, Malaysia, using Landsat-based temporal segmentation (LandTrendr) of the Normalized Burn Ratio (NBR) and the Normalized Difference Moisture Index (NDMI). Bin-stratified logistic regression models were fitted to quantify associations between disturbance occurrence and event-year anomalies in climate (precipitation, shortwave radiation, minimum temperature, vapour pressure deficit), canopy condition proxies (kernel NDVI, kNDVI), satellite/model-derived productivity (net primary productivity, NPP), and anthropogenic accessibility (distance to roads, open water, mangrove edge, and built-up intensity). Disturbance area and patch density increased abruptly after 2010, with most mapped events being small (<3 ha) and spatially dispersed. In a model-based dominance analysis (dominant linear-predictor contribution by group), the largest share of disturbed pixels was most strongly associated with productivity/greenness anomalies (≈51.6% of the filtered disturbed footprint), followed by climate anomalies (≈26.6%) and anthropogenic accessibility (≈21.8%). Negative kNDVI anomalies were associated with substantially lower odds of disturbance (odds ratio ≈ 0.097), whereas positive NPP anomalies were associated with higher odds (OR ≈ 1.31). Brighter and drier-than-average conditions (higher shortwave radiation and positive precipitation anomaly, as defined here) corresponded to higher disturbance odds, while cooler night-time conditions were associated with lower odds. Among accessibility covariates, proximity to roads showed a strong association with higher disturbance probability, whereas built-up intensity was not significant after accounting for distance gradients. Overall, the results provide an association-based framework for prioritising monitoring and management by jointly considering climate variability, canopy-condition signals, and access corridors.

1. Introduction

Mangrove forests are among the most productive and valuable ecosystems on Earth. They occupy tropical and subtropical coastlines and estuaries, forming biodiversity hotspots and delivering essential services to human societies. Recent syntheses highlight that mangroves sustain coastal fisheries. Approximately 4.1 million small-scale fishers operate primarily in mangrove areas (Ghosh et al., 2022), and mangroves act as natural buffers that reduce storm damage, saving an estimated USD 65 billion in property damage and shielding 15 million people from flooding annually (Hu et al., 2023). Their blue carbon potential is remarkable; waterlogged soils allow mangrove forests to convert carbon dioxide to organic carbon up to four times more efficiently than many terrestrial forests, resulting in global storage of about 22.86 gigatons of CO_2, 87 % of which resides in soils (Araya-Lopez et al., 2023). Degradation of mangroves, therefore, has disproportionate consequences for climate mitigation (Sun et al., 2023), while the loss of habitat undermines fisheries, coastal protection, and cultural livelihoods. Recognizing their importance, international frameworks such as the United Nations Decade on Ecosystem Restoration and the Global Mangrove Alliance set ambitious targets to halt further loss, restore 4000 km^2 of mangroves by 2030, and double protected area coverage (Husna et al.,

* Corresponding author.
E-mail address: zali_johari@upm.edu.my (S. Johari).

https://doi.org/10.1016/j.tfp.2026.101326

Available online 1 June 2026

2023).

Despite these initiatives, mangrove ecosystems continue to decline. Remote sensing assessments estimate that 25–50 % of global mangrove area has been lost since 1980 (Schürholz et al., 2023), and approximately 30 % has been lost in the past four decades (Sun et al., 2023). Eleven of the world's 70 mangrove species, **16%**, are now threatened with extinction (Dermawan et al., 2024). The primary drivers of this decline are anthropogenic: conversion for aquaculture, oil palm cultivation, and rice cultivation caused 43% of global mangrove loss between 2000 and 2020. Aquaculture alone accounted for around 31 % of losses during 2000–2010, though its importance declined to 21 % in 2010–2020 as oil palm conversion increased from 4 % to 14 % (Gou et al., 2024). In addition to aquaculture and agricultural expansion, mangroves have also been converted or degraded by coastal development linked to tourism, including the construction and operation of resort and recreational infrastructure and associated activities (Blanton et al., 2024; Singgalen, 2022). Natural retraction due to sea-level rise, coastal erosion, and other climate-change impacts contributed to another 26 % of losses (Bennett et al., 2024), reflecting the rising influence of climate on mangrove persistence. These drivers vary by region; South and Southeast Asia remain the global epicenter of anthropogenic mangrove loss, where aquaculture accounts for 35 % of regional loss and natural retraction 17 %, whereas oil-palm and rice conversion are also significant (Wang et al., 2024). The intensifying frequency of extreme events and sea-level rise further threatens mangrove resilience by increasing natural retraction (Dong et al., 2024).

Advances in remote sensing have revolutionized our ability to map and monitor ecosystems and their dynamics (Anees et al., 2024a; Mehmood et al., 2024b). Traditionally, mangrove inventories relied on manual interpretation of aerial photographs; however, the proliferation of multispectral and radar satellite data has enabled global mapping at resolutions of 10–30 meters. LandTrendr and related Landsat time-series algorithms can detect abrupt spectral trajectory changes consistent with disturbance and recovery dynamics, while synthetic aperture radar can capture canopy structure and hydroperiod/inundation signals (Kennedy et al., 2010; Zhu and Woodcock, 2014). A 2024 FAO manual outlines how optical, radar, LiDAR, and uncrewed aerial systems can be combined to monitor mangroves at fine scales (Mugiraneza et al., 2020). At the same time, machine learning approaches are enhancing classification accuracy (Anees et al., 2024b, 2025c; Mehmood et al., 2024a). For example, a UNet++ deep learning model was applied to Sentinel-2 data to monitor mangroves in the United Arab Emirates, achieving a mean Intersection-over-Union **score** of 87.8%. They noted that the global mangrove area had declined by 25–50% since 1980 (Pasquarella et al., 2022) and emphasized that deep learning methods outperform traditional classifiers (Gelabert et al., 2021). Such progress underscores the promise of automated disturbance detection; yet most studies focus on mapping mangrove extent/cover (or broad vegetation/land-cover classes) rather than linking disturbance events to their underlying climatic and socio-economic drivers (Anees et al., 2025a).

The drivers of mangrove loss in Sarawak, Malaysia, remain poorly understood, despite the state harboring some of Borneo's most extensive mangrove stands. Existing global and regional analyses highlight that anthropogenic activities, particularly aquaculture and agriculture, dominate the loss in Southeast Asia (Anees et al., 2025b, 2025d; Khan et al., 2024, 2025; Pérez et al., 2022; Shahzad et al., 2025a; Shahzad et al., 2025b; Xiong et al., 2024), but they seldom disentangle the relative roles of climate variability, productivity anomalies, and accessibility in driving fine-scale disturbance. Moreover, while machine-learning and time-series techniques have been used to classify mangrove cover, few studies have quantified how climate anomalies (precipitation, temperature, and radiation), net primary productivity, and human proximity interact to influence the likelihood of disturbance (Mehmood et al., 2024c). Addressing this gap is crucial for climate adaptation and the design of targeted conservation measures.

This study aims to fill that gap by combining multidecadal Landsat time series, high-resolution climatic and productivity data, and anthropogenic covariates to identify and interpret mangrove disturbances in Sarawak. Specifically, our objectives were **(**1) to map the spatial and temporal patterns of mangrove disturbance using a LandTrendr segmentation of Normalized Burn Ratio (NBR) and Normalized Difference Moisture Index (NDMI) time series; (2) to quantify the relative contributions of climatic anomalies, productivity anomalies and anthropogenic factors to disturbance probability using logistic regression and dominance analyses; and (3) to assess how these drivers vary across time-since-disturbance and along gradients of accessibility. By linking remote sensing to ecological processes, this work provides a comprehensive framework to understand mangrove vulnerability and informs management strategies for conserving these critical ecosystems.

2. Methods and materials

2.1. Study area

The study domain encompasses the mangrove belt of Sarawak, Malaysia Borneo, along the South China Sea, spanning approximately 1.5–5.0° N and 109.6–114.4° E (centroid ≈ 3.0° N, 113.0° E) (Fig. 1). Mangroves fringe a series of tide-influenced estuaries and deltas, including the Rajang–Igan–Saribas complex in the southwest and the Baram system in the northeast, set within a low-relief coastal plain dissected by distributary channels and tidal creeks (Alam et al., 2012). Substrates are dominantly fine alluvium and peat-rich muds that favor *Rhizophora–Bruguiera* forest mosaics, with *Avicennia, Sonneratia*, and *Nypa fruticans* occupying more open, fluvial, and upstream brackish reaches (Lestari et al., 2024; Wolswijk et al., 2020). Climatically, Sarawak is characterized as equatorial–monsoonal, with consistently warm temperatures and high humidity. Seasonal shifts in cloudiness and rainfall generate pronounced variability in shortwave radiation and atmospheric dryness (VPD), which in turn modulate canopy condition and productivity (Mehmood et al., 2025a; Mitra et al., 2023, 2025c). Freshwater and sediment inputs from large river catchments maintain estuarine gradients and drive along-shore heterogeneity in salinity, turbidity, and nutrient supply. The human footprint is spatially heterogeneous across the coastal zone: protected areas and state lands occur alongside rapidly modified production landscapes. High-resolution imagery indicates dense road development and extensive plantation/agricultural matrices in parts of Sarawak's coastal plain (e.g., in the broader Bintulu region), generating strong accessibility gradients and edge fragmentation within and around mangrove stands. These socio-ecological contrasts are expressed at landscape scales relevant to patch formation, edge dynamics, and early regrowth.

Sarawak was selected because it is ecologically consequential, its mangroves support fisheries, shoreline protection, and carbon storage across intense exposure and freshwater gradients (FAO, 2023)**.** It also offers a realistic interface between climatic vulnerability (radiation and moisture anomalies) and anthropogenic pressure (selective extraction, small-scale clearing, aquaculture), typically producing small, dispersed disturbance patches (Songsom et al., 2019). Finally, heterogeneous governance of protected areas alongside working landscapes enable policy-relevant contrasts in susceptibility and recovery. Together, these features make Sarawak a diagnostically rich and generalizable setting for identifying where and when mangrove canopies are most vulnerable.

2.2. Datasets and pre-processing

Analyses were confined to a mangrove footprint sourced from Global Mangrove Watch (GMW; v3.0, 2020 epoch) (Bunting et al., 2022) and rasterised to a common 30 m WGS-84 grid; this grid served as the reference for all layers, with non-mangrove pixels set to NA. Landsat Collection-2 Surface Reflectance (TM/ETM+/OLI/OLI-2) scenes (1990–2023) were composited for the core growing season (20 June–20 September) after QA removal of clouds, shadows, and cirrus, together

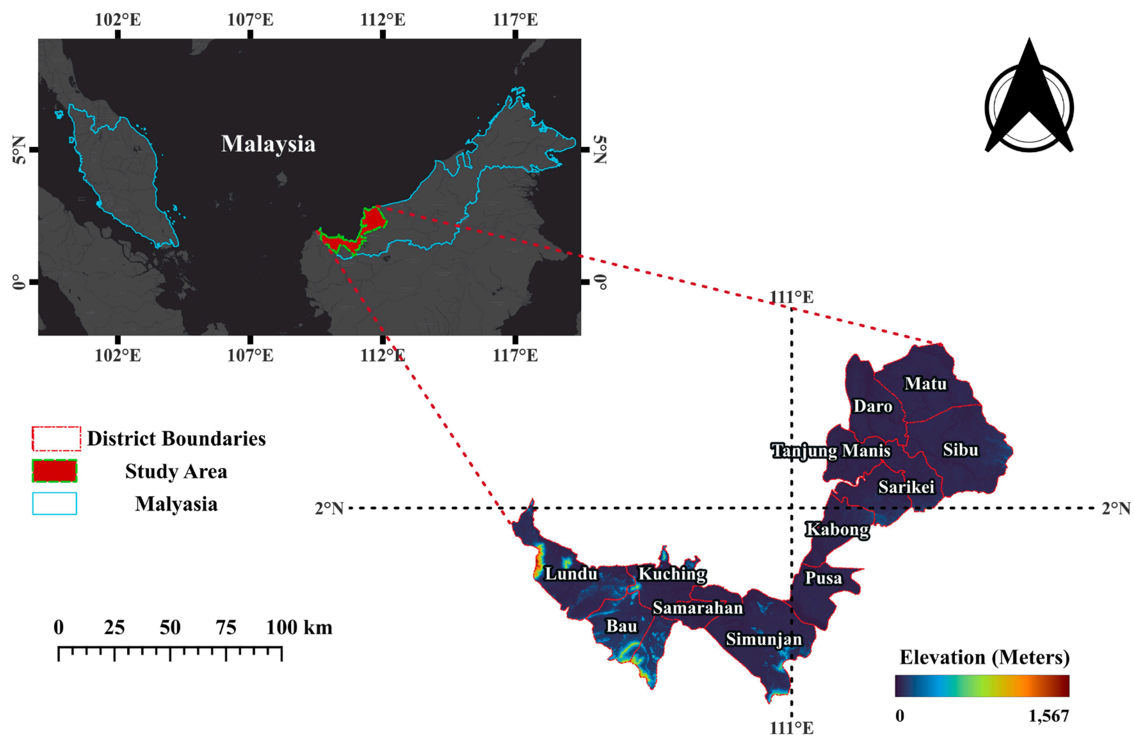

Fig. 1. Location of the study area in Sarawak, Malaysia. The inset situates Sarawak within Malaysia, highlighting the study area. The main panel maps coastal districts and labels key administrative units; district boundaries are shown with red dashed lines.

with NDWI-based water screening (Li et al., 2013). Annual robust-median composites yielded kernel NDVI (kNDVI) and the supporting indices Normalized Difference Moisture Index (NDMI) and Normalized Burn Ratio (NBR), all aligned to the 30 m grid (Wang et al., 2024). Net primary productivity (NPP) was obtained from MODIS MOD17A3HGF (500 m, 2000–2023), quality-filtered, and bilinearly resampled to the common 30 m grid for joint analysis.

Climatic covariates included shortwave radiation (SRAD), maximum temperature (TMAX), minimum temperature (TMIN), vapour pressure deficit (VPD), vapour pressure (VAP), precipitation (PR), climatic water deficit (DEF), and 10 m wind speed (VS), compiled from TerraClimate and ERA5-Land (Abatzoglou et al., 2018). Monthly fields were aggregated to annual growing season means, with sums used for precipitation and climatic water deficit, and then reprojected and resampled to the 30 m analysis grid. These variables were subsequently expressed as standardised interannual anomalies (z-scores) relative to the 1990–2023 climatology (Mehmood et al., 2025b) (Table S1). Because the native climate grids are substantially coarser than the Landsat-based analysis grid, resampling to 30 m was performed only to ensure spatial co-registration and consistent extraction within the mangrove mask; it did not increase the intrinsic spatial detail of the climate data. Accordingly, the climatic predictors were interpreted as broad-scale background forcings rather than as fine-scale microclimatic measurements, and any unresolved local heterogeneity is acknowledged as a limitation of the analysis. Anthropogenic context combined the Global Human Settlement Layer (GHSL) built-up and population grids with proximity surfaces derived from OpenStreetMap features; Euclidean distance-to-feature rasters (in metres) to the nearest road and settlement were computed on the 30 m grid within the mangrove analysis mask (mangrove extent intersected with the Sarawak coastal study boundary) and log-transformed (Anees et al., 2025a). Harmonisation used bilinear resampling for continuous fields and nearest-neighbour resampling for categorical or binary layers, and pixels lacking sufficient valid observations were excluded. LandTrendr summarised disturbance timing and shape using segment metrics, including year of disturbance, magnitude, duration, and the pre-disturbance baseline level of the stable segment immediately preceding change, derived from the annual NBR and NDMI stacks. Patches were then regularised using a minimum mapping unit of approximately 1 ha (Bunting et al., 2018, 2023). Finally, ridge/GAM coefficient surfaces were separated by effect direction (adverse versus beneficial, based on coefficient sign with respect to reduced canopy greenness or reduced estimated productivity), and the adverse-direction components were aggregated and min–max scaled within the mangrove mask to produce continuous vulnerability rasters for greenness (kNDVI) and estimated productivity (NPP), which were used in subsequent summaries and hotspot analyses. Fig. 2 summarises the end-to-end workflow from data harmonisation and seasonal compositing through disturbance detection, model-based attribution, and climate-response vulnerability mapping to derive management-ready spatial products.

2.3. *Persistent degradation mapping with landsat–landtrendr (1990–2023)*

Annual degradation layers were derived from Landsat Collection-2 Surface Reflectance (TM, ETM+, OLI, and OLI-2) data spanning the years 1990–2023. Yearly medians were generated within a fixed seasonal window (20 June–20 September) after removing clouds and shadows based on QA bands and masking per-scene inundation using the NDWI index (Gelabert et al., 2021). Two structure- and moisture-sensitive indices were selected for analysis (Kennedy et al., 2018) (Eq. (1) & 2).

$$\mathrm{NBR} = \frac{\rho_{\mathrm{NIR}} - \rho_{\mathrm{SWIR2}}}{\rho_{\mathrm{NIR}} + \rho_{\mathrm{SWIR2}}} \tag{1}$$

$$\mathrm{NDMI} = \frac{\rho_{\mathrm{NIR}} - \rho_{\mathrm{SWIR1}}}{\rho_{\mathrm{NIR}} + \rho_{\mathrm{SWIR1}}}. \tag{2}$$

Time-series trajectories were segmented with LandTrendr using the following settings: maxSegment = 7, spikeThreshold = 0.95, vertexCountOvershoot = 4, preventOneYearRecovery = true, recoveryThreshold = 0.33, pvalThreshold = 0.05, bestModelProportion = 0.85, and minObservationsNeeded = 6. These parameters were selected after

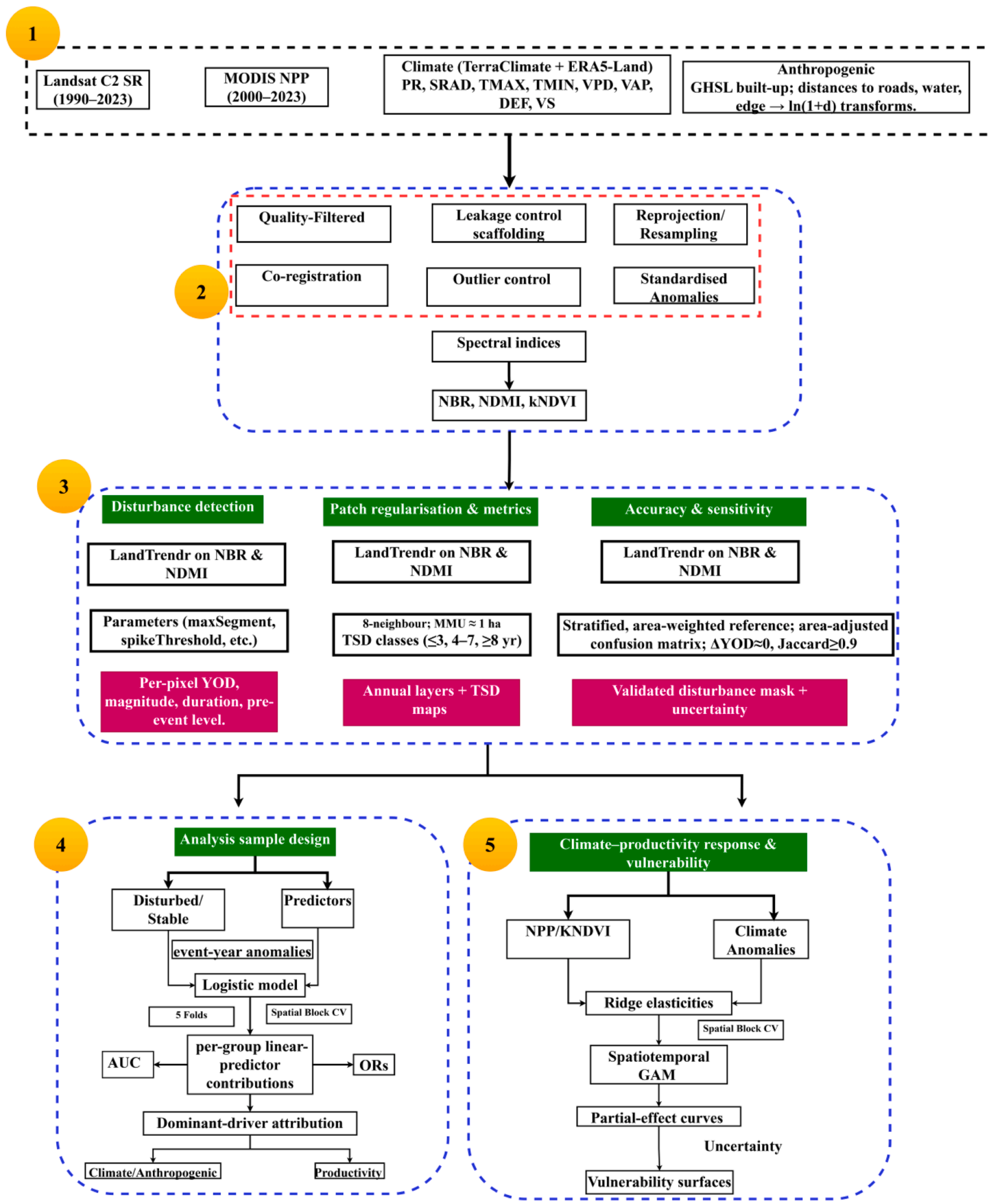

Fig. 2. Workflow for diagnosing mangrove canopy degradation and climate sensitivity in Sarawak.

systematic testing of alternative configurations to balance specificity and stability in tidally influenced mangroves (Kennedy et al., 2018) (Table S2). The adopted configuration suppresses one-year artefacts, limits over-segmentation, and preserves multi-episode disturbance trajectories. From the fitted trajectories, per-pixel year of detection (YOD), magnitude of change ($|\Delta I|$), duration, and pre-event index level (I_{pre}) were extracted. Because objective was to map persistent mangrove degradation (i.e., canopy loss or sustained decline that does not recover over the short-to-intermediate term), an explicit persistence criterion was applied. This design intentionally excludes short-lived disturbances followed by rapid recovery (e.g., brief defoliation or transient sediment/water effects) and therefore the resulting layer should be interpreted as persistent/ongoing degradation (or likely loss), not as a complete inventory of all mangrove disturbances. A pixel was classified as persistently degraded when both indices satisfied $|\Delta I| \geq 200$, duration ≤ 4 years, $I_{\text{pre}} \geq 300$, and a persistence condition requiring that index recovery during the subsequent three years remained below 70% of the pre-event value, consistent with non-recovery over the evaluation window (Kennedy et al., 2010; Qiu et al., 2023). The earliest breakpoint meeting these conditions was recorded as YOD. Spatial filtering was applied through an 8-neighbour connected-component rule with a minimum mapping unit of 11 pixels (~1 ha). Retained patches carried four attributes: YOD, $|\Delta I|$, duration, and I_{pre} (Mugiraneza et al., 2020).

Robustness was assessed by perturbing disturbance thresholds (±20% on $|\Delta I|$; duration ≤ 5 years), widening the seasonal compositing window (May–November), and testing single-index variants. In addition, sensitivity to LandTrendr control parameters was evaluated by varying each setting individually and as a combined recommended configuration (Ding and Li, 2023). These trials confirmed the stability of degraded area estimates and timing (Table S3). Accuracy evaluation followed a stratified, area-weighted sampling design that combined mapped class (persistently degraded/non-degraded), disturbance magnitude, and geomorphic sector. Each sample was interpreted in relation to time-adjacent Sentinel-2 and high-resolution basemaps, with the interpreter's confidence level recorded. The full reference sampling scheme is detailed in Table S4. Area-adjusted users' and producers' accuracies were derived from the comparison, and year-of-detection agreement was assessed by comparing mapped and reference YOD values (Wang et al., 2023). The area-adjusted confusion matrix is provided in Table S5. All analyses were restricted to a strict 0/1 mangrove mask. The binary mask was aligned to the LandTrendr grid using nearest-neighbour resampling and converted to 1/NA format to prevent class bleed. Total mangrove area on the analysis grid was 1114.7 km^2, consistent with the native mask (drift = 0.04%).

Patch metrics were computed annually. For each year, the unfiltered set comprised all mangrove pixels with YOD equal to that year. Binary rasters were generated, and patches were delineated using 8-neighbour connectivity. Three metrics were derived: (i) disturbed area (km^2), (ii) patch density (patches km^{-2} relative to mangrove area), and (iii) mean patch size (ha). A filtered series was also derived by applying minimum thresholds (magnitude ≥ mangrove-wide 75th percentile, duration ≤ 2 years, patch size ≥ 3 pixels). Pre- and post-2010 summaries were compiled, and monotonic trends in annual disturbed area share (% of mangrove extent) were evaluated using Kendall's τ (Liu et al., 2023). Time-since-disturbance (TSD) classes were additionally mapped to distinguish recent (≤ 3 years), intermediate (4–7 years), and older (≥ 8 years) events, with area shares summarized in Figure S1.

2.4. Drivers of degradation: covariates, sampling, and modelling

All predictors were co-registered to the LandTrendr grid (WGS-84; native Landsat 30 m) and clipped with a strict 1/NA mangrove mask. Continuous rasters used bilinear resampling and classes were aligned on their native grid before masking. Disturbance inputs comprised the earliest filtered YOD and an ever-disturbed mask; "stable" pixels are those with no disturbance during 1991–2023. Annual stacks (2001–2023) were summarized as long-term means for DEF, PR, SRAD, TMAX, TMIN, VAP, VPD, and VS. kNDVI and MODIS NPP were likewise averaged over 2001–2023. Built-environment pressure was represented by GHSL-derived mean built-up intensity (BU). Proximity covariates were Euclidean distances to roads (D_ROAD), open water (D_WATER), and the mangrove edge (D_EDGE), entered as ln(1 + d) to temper leverage. Event-time conditions and anomalies were extracted at the disturbance year t_0 for disturbed samples (Gou et al., 2024). For each variable X, the anomaly was defined as the deviation between the long-term mean and the event-year value (Eq. (3)).

$$\Delta X = \overline{X}_{2001-2023} - X_{t_0} \tag{3}$$

Positive ΔX therefore indicates that the event-year value is below its long-term mean (e.g., ΔPR > 0 denotes drier-than-average conditions at t_0). The resulting predictor set comprised climatic anomalies (ΔDEF, ΔPR, ΔSRAD, ΔTMAX, ΔTMIN, ΔVAP, ΔVPD, ΔVS), productivity anomalies (ΔkNDVI, ΔNPP), BU, and transformed distances $ln(1 + DROAD)$, ln (1 + D_WATER), ln (1 + D_EDGE). For stable samples, a pseudo-event year $t_0$was used solely for extracting anomalies to ensure temporal comparability (Wang et al., 2024).

A balanced sample was drawn within the mangrove mask using two strata: Disturbed pixels flagged by the filtered disturbance mask, with t_0 given by the earliest filtered YOD; and Stable pixels with no disturbance over 1991–2023. Samples inheriting any missing predictor after masking/alignment were excluded. Disturbance timing was stratified into five intervals to reflect the post-2010 escalation while preserving adequate sample sizes in early years: ≤ 2009, 2010–2012, 2013–2016, 2017–2019, and 2020–2023. The pre-2010 interval was kept broad due to sparse early events; where the 2006–2009 share exceeded 5% of disturbed pixels, this interval was split into ≤ 2005 and 2006–2009. Stable samples were assigned a bin-midpoint pseudo-year for anomaly extraction (2007 for ≤ 2009; 2011, 2014, 2018, 2022 for subsequent bins). Disturbed samples always used their actual t_0 from the earliest filtered YOD.

2.4.1. Statistical model and evaluation

Binary outcomes (disturbed vs. stable) were modelled using logistic regression with bin fixed effects (Mihi et al., 2022) (Eq. (4)),

$$\Pr(\text{disturbed}) = \text{logit}^{-1}(\alpha + \beta^{\top}\boldsymbol{x} + \gamma_{\text{bin}}), \tag{4}$$

where $x$contains the standardised predictors listed above. Predictors were z-scored before fitting so that coefficients are on a comparable scale. Model skill was assessed with 5-fold stratified cross-validation (strata = class × bin), reporting the area under the ROC curve (AUC) (Bey et al., 2020; Szeghalmy and Fazekas, 2023). To reduce leakage from spatial autocorrelation, spatial block cross-validation was additionally conducted. The mangrove domain was tessellated into ∼10 km square blocks in a projected, metric coordinate reference system (CRS); k = 5folds were assigned at the block level, so each held-out fold formed a contiguous geographic unit. All tuning and evaluation were nested in this scheme. Block-CV AUC refers to AUC computed from predictions evaluated on held-out spatial blocks (i.e., out-of-block validation), and is reported as the primary discrimination metric, alongside Brier score and calibration intercept/slope (Fig. S4). Coefficients are presented as odds ratios with 95% Wald intervals (Tables S6a–S6b).

For interpretation, contributions to the linear predictor $\beta_j x_j$ were summed within three groups: Climate ($\Delta DEF - \Delta VS$), Productivity ($\Delta kNDVI$, ΔNPP), and Anthropogenic (BU, ln(1+D_ROAD), ln (1+D_WATER), ln(1+D_EDGE). The group with the largest positive contribution in the sample was labelled the dominant driver; ties or non-positive totals were marked neutral. These labels facilitate the subsequent mapping of dominant-driver zones by a majority vote within disturbed patches.

2.5. Climate–productivity response and vulnerability

Analyses utilized the same reference grid and mangrove mask described above. All annual stacks were co-registered, clipped, and reduced to their common temporal overlap, with pixels exhibiting zero temporal variance being excluded. Let Y_{it} denote kNDVI or NPP at pixel i and year t; let X_{jit} denote the eight climate forcings ($j \in DEF, PR, SRAD, TMAX, TMIN, VAP, VPD, VS\}$). To place effects on a comparable, unitless scale, each series was standardised per pixel across time (Eq. (5)).

$$\widetilde{Y_{it}} = \frac{Y_{it} - \overline{Y_i}}{s_{Y,i}}, \qquad \widetilde{X_{jit}} = \frac{X_{jit} - \overline{X_{j,i}}}{s_{X_j,i}} \tag{5}$$

so, coefficients are elasticities: the change (in SD, i.e., standard deviations, of Y) per one-SD change in a covariate, conditional on the others. Pixel-wise ridge regression estimated simultaneous linear effects of the eight forcings on productivity (Eq. (6)).

$$\widehat{\beta}_i(\lambda) = \boldsymbol{argmin}_{\beta} \sum_{t \in T_i} \left(\widetilde{Y}_{it} - \sum_j \widetilde{X}_{jit}\beta_j \right)^2 + \lambda \| \beta \|_2^2 \tag{6}$$

yielding coefficient maps $\widehat{\beta_{ij}}$ and goodness-of-fit (Eq. (7)).

$$R_i^2 = 1 - \frac{\sum_t (\widetilde{Y_{it}} - \widehat{\widetilde{Y}_{it}})^2}{\sum_t (\widetilde{Y_{it}} - \overline{\widetilde{Y}_i})^2} (\overline{\widetilde{Y}_i} \approx 0) \tag{7}$$

To avoid confusion with the disturbance-probability model in Section 2.4.1, the climate–productivity analysis was not fitted using logistic regression. Instead, pixel-wise ridge regression was used for continuous responses (kNDVI and NPP), and the regularisation parameter (λ) was selected by 5-fold cross-validation using mean squared error (MSE). To stabilize estimates under collinearity (PR–VPD–SRAD), λ was chosen by 5-fold cross-validation along the time axis on a random subset of pixels; the selected $\lambda^{\star}$ was then applied to all pixels for each response. Potential nonlinearity was assessed with a complementary spatiotemporal generalized additive model (GAM) fitted on a stratified panel (sampled pixels, all years) (Eq. (8)).

$$\widetilde{Y_{it}} = \alpha + \sum_j s_j\left(\widetilde{X_{jit}}\right) + s(x_i, y_i) + \varepsilon_{it} \tag{8}$$

where $s_j(\cdot)$are thin-plate splines (moderate basis; smoothing parameters estimated by restricted maximum likelihood, REML) and $s(x, y)$absorbs broad spatial structure. Partial-effect curves s_j (with pointwise intervals) provide distribution-free evidence for thresholds or saturation beyond the linear ridge elasticities. Generalization of the GAM partial effects was quantified using 5-fold spatial block cross-validation (~10 km) on the sampled panel (Yang et al., 2012). Pixel IDs were grouped by block and all years for a pixel were kept within the same fold. From out-of-fold predictions RMSE, R^2, calibration intercept/slope, and 95% prediction-interval coverage were summarized.

Vulnerability was derived by aggregating ridge elasticities in the expected harm direction. For pixel i (Eq. (9)).

$$v_i = \sum_{j \in H^+} \max\left(0, \widehat{\beta_{ij}}\right) + \sum_{j \in H^-} \max\left(0, -\widehat{\beta_{ij}}\right) \tag{9}$$

with $H^+ = \{SRAD, VPD, DEF, TMAX, VS\}$ and $H^- = \{PR, VAP, TMIN\}$. This raw score was min–max scaled over the mangrove domain (Eq. (10)).

$$V_i = \frac{v_i - \min\limits_{\Omega}(v)}{\max\limits_{\Omega}(v) - \min\limits_{\Omega}(v)} \in [0, 1] \tag{10}$$

producing continuous greenness and productivity vulnerability surfaces. Pixels lacking sufficient temporal support remain NA.

3. Results

3.1. Mangrove disturbance trajectories (1991–2023): from low activity to fragmented peaks

Within the mapped mangrove extent of 1114.7 km², the LandTrendr results indicate a marked increase in disturbance after 2010 (Fig. 3A). Across 1991–2023, the unfiltered cumulative disturbed area was 132.49 km², representing 11.89% of the mapped mangrove area. Before 2010, disturbance totalled 22.38 km² (2.01%) across 3360 patches, with an aggregate density of 3.01 patches km^{-2} and a mean patch size of 0.67 ha. From 2010 to 2023, disturbed area increased to 110.11 km² (9.88%) across 4726 patches, with patch density rising to 4.24 patches km^{-2} and

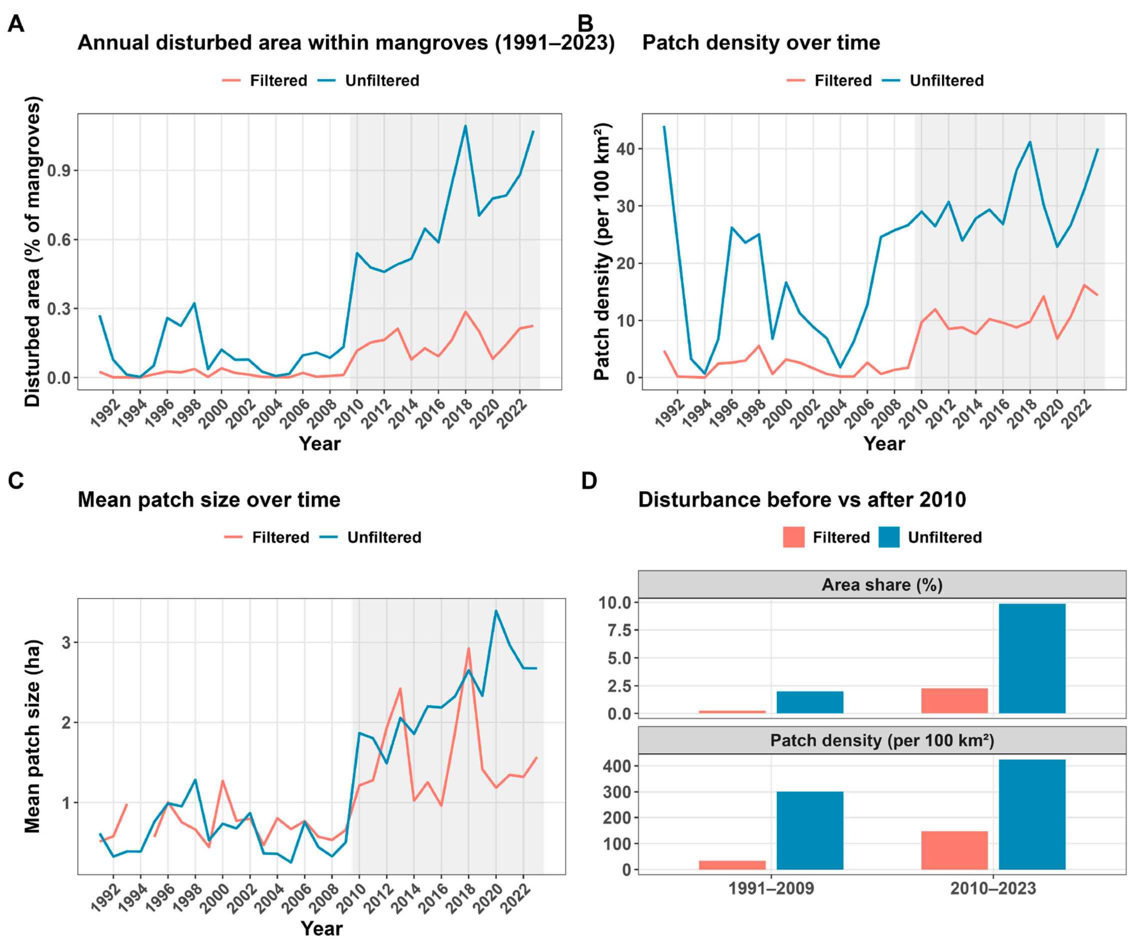

Fig. 3. Composite panels (A–D): (A) annual disturbed area (% of mangroves) with post-2010 shading; (B) patch density (per 100 km²); (C) mean patch size (ha); and (D) pre- versus post-2010 summaries of area share and patch density for the unfiltered and filtered series. “Unfiltered” denotes all LandTrendr detections meeting the base change criteria, whereas “filtered” denotes detections retained after applying light post-processing constraints (magnitude ≥ Q75, duration ≤ 2 years, and minimum patch size ≥ 3 pixels) to reduce small or short-lived artefacts.

mean patch size to 2.33 ha. The annual disturbed-area share increased significantly through time ($\tau = 0.617$, $p = 4.8 \times 10^{-7}$), with distinct peaks in 2017–2018 and persistently elevated levels through 2023 (Fig. 3A–B). Applying light post-processing filters (mag $\geq$ Q75, dur $\leq$ 2 yr, and patch size $\geq$ 3 px) reduced the cumulative disturbed area to 28.02 km^2 (2.51%), but the temporal pattern remained unchanged. Under the filtered series, disturbance totalled 2.78 km^2 (0.25%) during 1991–2009 and 25.24 km^2 (2.26%) during 2010–2023, with a continued upward trend over time ($\tau = 0.545$, $p = 8.7 \times 10^{-6}$). Patch density increased alongside disturbed area, whereas mean patch size remained relatively small, generally around 1–3 ha during the more active years (Fig. 3C). This pattern indicates that the post-2010 increase was characterised mainly by a greater number of relatively small disturbance patches rather than by a small number of large clearings. The contrast between the pre-2010 and post-2010 periods is summarised in Fig. 3D for both the unfiltered and filtered series. Sensitivity analyses further showed that disturbed area and patch counts were stable across alternative parameterisations, with ΔYOD $\approx$ 0 and Jaccard agreement $\geq$ 0.90 between the baseline disturbance mask and those generated under alternative thresholds and settings (Table S2).

3.1.1. Time-since-disturbance (TSD)

The time-since-disturbance (TSD) analysis showed that 39.22 km^2 of mangroves (3.52% of the mapped extent) were disturbed within the last 3 years, 35.98 km^2 (3.23%) were disturbed 4–7 years ago, and 57.30 km^2 (5.14%) were disturbed 8 or more years ago. Together, these classes sum to 132.49 km^2, equivalent to 11.89% of the mapped mangrove area. Disturbance within the last 7 years accounted for 6.75% of the mangrove extent, consistent with the post-2010 increase shown by the annual patch metrics (Fig. 3A–D). TSD was calculated from the earliest filtered year-of-disturbance (YOD) surface. The classed TSD map is presented in Fig. 4A, the corresponding area shares are shown in Figure S1, and the continuous TSD raster is provided in Fig. 4B These results add a temporal dimension to the patch analysis by showing how the disturbed area is distributed across recent, intermediate, and older disturbance classes. In this study, the $\leq$3 year, 4–7 year, and $\geq$8-year categories are used as operational classes of disturbance recency rather than as direct evidence of ecological succession, recovery stage, or long-term degradation status. The TSD results therefore provide a concise temporal summary of disturbance patterns across the mangrove domain and complement the area- and patch-based trends presented above. Their main value lies in supporting temporal characterization of disturbance and helping to identify where disturbance has occurred more recently versus where it reflects older events.

Independent visual interpretation supported the reliability of the mapped degradation patterns. The stratified reference dataset (Table S5) yielded an overall accuracy of 0.865 (95% CI: 0.835–0.892), with user's and producer's accuracies for the degraded class close to 0.8 and a median YOD deviation of 0 years. These results are consistent with dual-index LandTrendr applications in humid, tidally influenced mangroves and indicate that the observed post-2010 increase reflects a stable disturbance signal rather than a parameterisation artefact.

3.2. Drivers of mangrove degradation: model performance and covariate effects

Disturbance probability was modeled using a bin-stratified logistic regression with standardized climatic and productivity anomalies (Δ variables), mean built-up intensity, and ln-transformed distance covariates. The model showed intense discrimination (5-fold CV AUC = 0.908 $\pm$ 0.004; Fig. 5A) and comparable skill across disturbance-timing bins ($\leq$2005: 0.909; 2006–2010: 0.923; 2011–2016: 0.910; $\geq$2017: 0.888; Table S6a). Cross-validated predictions displayed well-separated probability distributions for stable versus disturbed samples (Fig. 5B), supporting interpretation of the fitted coefficients. Standardized odds ratios (OR; per-SD change) indicate that the strongest associations (predictive effects) were with productivity anomalies and a subset of climatic variables (Fig. 6; Table S6b). The kNDVI anomaly was the strongest predictor in absolute terms (OR = 0.097, 95% CI: 0.088–0.107), with lower disturbance odds associated with greener-than-average conditions and higher odds associated with greenness deficits around the event year**.** The NPP anomaly increased disturbance odds (OR = 1.307, 1.216–1.405). Among climate years that were drier than average (ΔPR > 0) and brighter (ΔSRAD) were associated with higher odds (ΔPR OR = 1.229, 1.102–1.370; ΔSRAD OR = 1.482, 1.320–1.665 Cooler nighttime conditions (ΔTMIN) appeared to be protective (OR = 0.804, 0.658–0.982), while other atmospheric terms (ΔVPD, ΔVAP, ΔTMAX) were not significant. Within anthropogenic pressures, accessibility showed the most precise pattern: odds of disturbance decreased steeply with distance to roads (ln (1 + D_ROAD) OR = 0.380, 0.356–0.405), whereas distance to open water and to the mangrove edge showed more modest positive associations (ln (1 +

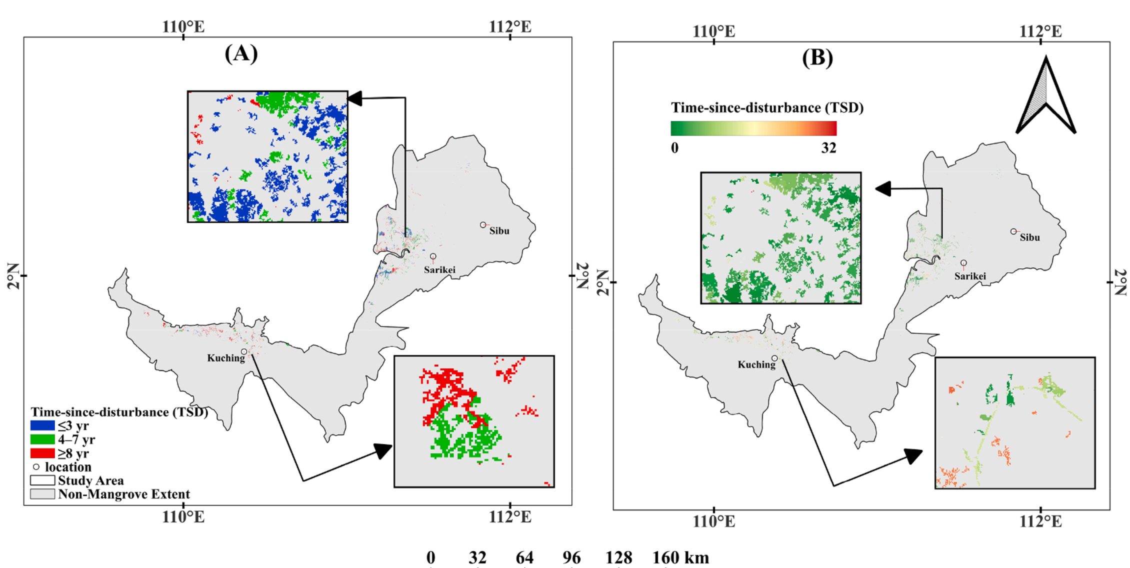

Fig. 4. Time-since-disturbance (TSD) in mangroves, reference year 2023. (A) Classed TSD showing pixels disturbed within $\leq$3 years, 4–7 years, and $\geq$8 years; pixels with no mapped disturbance during 1991–2023 are left blank, and non-mangrove areas are masked. (B) Continuous TSD (0–32 years; 0 = events in 2023, larger values = older events) rendered with a linear colour ramp. Both panels share the LandTrendr analysis grid, extent, and projection.

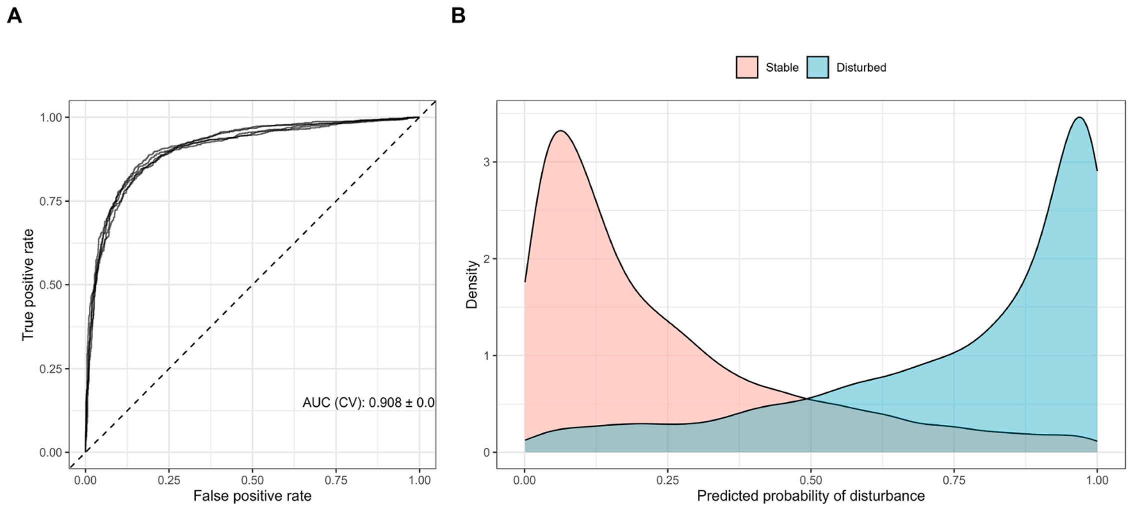

Fig. 5. Model discrimination and prediction separability. (A) Receiver operating characteristic (ROC) curves from 5-fold stratified cross-validation of the baseline logistic model (bin fixed effects; standardized climatic and productivity anomalies, GHSL built-up, and ln-distance covariates). Thin grey lines show individual folds; the bold curve is the mean. Mean AUC ± s.d. = 0.908 ± 0.004; the dashed diagonal denotes no-skill. (B) Densities of cross-validated predicted probabilities pooled across folds for Stable (pink) and Disturbed (teal) samples, illustrating strong separation with limited overlap near 0.5.

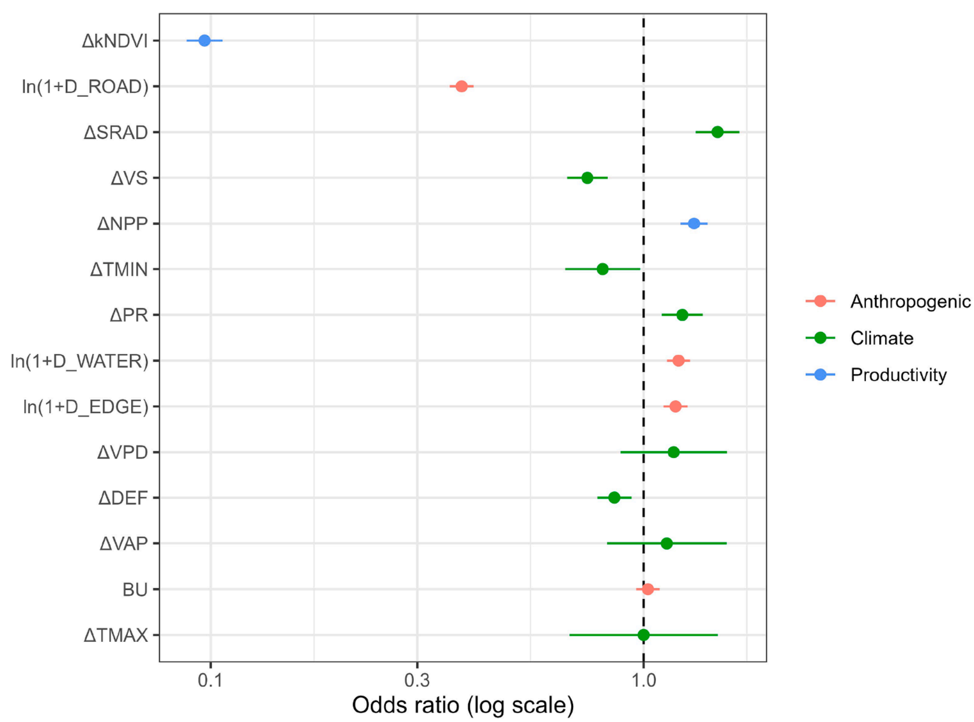

Fig. 6. Standardized effects on the odds of disturbance. Odds ratios (OR; log scale) and 95% Wald confidence intervals from the complete logistic model with bin fixed effects. Dots are point estimates; horizontal bars are 95% CIs; the dashed vertical line marks OR = 1 (no effect). Predictors were z-scored before fitting; distances entered as ln (1 + distance). Colors denote groups: Anthropogenic (red), Climate (green), and Productivity (blue). Numerical coefficients and CIs are reported in Table S6b, attribution of dominant drivers.

D_WATER) OR = 1.204, 1.132–1.280; ln (1 + D_EDGE) OR = 1.185, 1.112–1.264). Mean built-up intensity (BU) was not significant after controlling for distances and other covariates (OR = 1.023, $p = 0.470$).

Aggregating per-sample contributions (β·x) by group reveals that Productivity provided the dominant positive contribution for the majority of disturbed samples (56.3%), while Anthropogenic and Climate contributions each dominated approximately 22% (Fig. 7; Table S6c, S6d). The composition evolved through time: in the ≤2005 stratum, contributions were comparatively balanced (Productivity 38%, Anthropogenic 36%, Climate 26%); 2006–2010 saw Productivity strengthen (54%) with a still-substantial Anthropogenic share (31%); by 2011–2016, Productivity dominated (64%) with Climate secondary (29%) and a reduced Anthropogenic fraction (7%); in ≥2017, Productivity remained the leading contributor (69%) while Climate (18%) and Anthropogenic (13%) played more minor roles. The analysis indicates that canopy-condition departures (productivity anomalies captured by kNDVI and NPP) are the primary proximate signature of mangrove degradation events, with dry, high-radiation anomaly patterns acting as consistent secondary climatic co-factors. Anthropogenic influence is most clearly expressed via proximity to roads, a strong spatial gradient

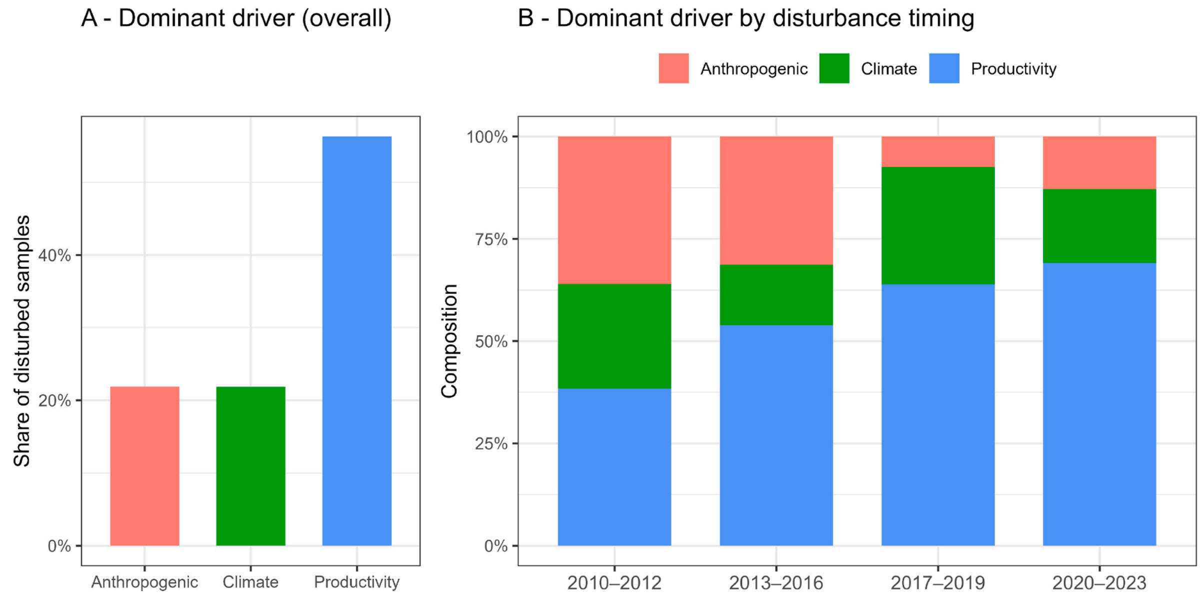

Fig. 7. Dominant drivers of mangrove disturbance. (A) Overall share of disturbed samples attributed to the dominant driver group. (B) Composition of dominant drivers by disturbance timing (year-of-detection; YOD). The dominant driver at each sample is the group with the most significant positive contribution to the logistic model's linear predictor (sum of β·x across variables within group).

that is more prominent in earlier events and remains detectable thereafter.

Using the pixel-wise dominant-driver map (Figure S2) restricted to the filtered disturbed footprint, productivity accounts for 14.46 km^2 (51.6%) of disturbed mangroves, climate for 7.46 km^2 (26.6%), and anthropogenic factors for 6.10 km^2 (21.8%), summing to 28.02 km^2 (i.e., the filtered cumulative disturbed area). These areal shares closely reflect the sample-level attribution (productivity ≈56%, climate/anthropogenic ≈22% each), reinforcing that departures in canopy productivity at the event year are the dominant proximate signature of disturbance, with secondary climatic and localized anthropogenic influences.

3.3. Climate–productivity sensitivity and spatial dominance

Interannual climate variability was related to mangrove productivity using ridge regression. The ridge penalty was tuned by 5-fold cross-validation across years and mean squared error (MSE) was used only for this tuning step. Cross-validated MSE decreased monotonically with stronger regularisation within the tested λ range and reached its minimum at the upper bound of the search grid for both responses ($\lambda = 5$). This pattern is consistent with the use of ridge regularisation under collinearity among climate predictors. The minimum MSE was 0.795 for NPP and 1.03 for kNDVI (Table S7; Fig. 8). Accordingly, ridge coefficients were mapped using $\lambda = 5$.

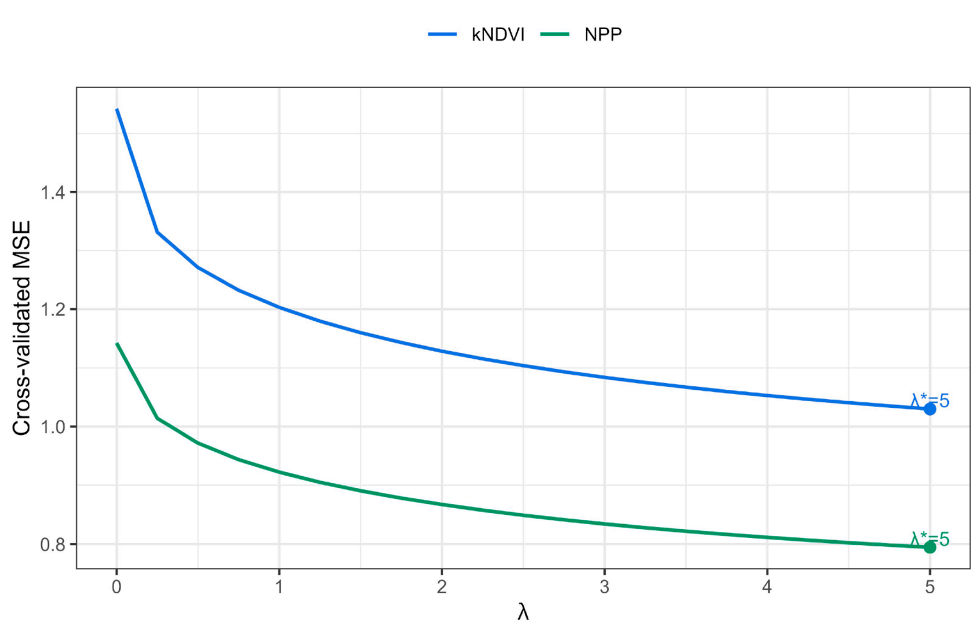

Fig. 8. Cross-validated mean squared error (MSE) used to tune the penalty parameter in the ridge-regression models relating interannual climate variability to kNDVI and NPP. This figure refers to ridge-regression tuning only, not to the logistic regression used for disturbance probability in Section 3.2. For both responses, MSE decreased monotonically within the tested λ range and reached its minimum at $\lambda = 5$.

3.4. Non-linear climate–productivity responses (GAMs)

Spatial generalized additive models (GAMs) were fitted to per-pixel standardised annual anomalies (z-scores; Eq. (5)), so both the climate covariates and the response are expressed in SD units. Fig. 9 shows GAM partial effects: in each panel, the x-axis is the standardised anomaly of a given climate covariate, and the y-axis is the centred smooth contribution $s_j(\cdot)$to the fitted kNDVI anomaly, conditional on the other covariates and the spatial smooth**.** Spatial GAMs fitted to annual anomalies showed that all climate smooths and the spatial term were highly significant. The model for kNDVI explained ≈11% of variance (adj. $R^2 = 0.109$; deviance explained = 10.9%), while the NPP model explained ≈40% (adj. $R^2 = 0.401$; deviance explained = 40.1%) (Fig. 9). Partial effects are broadly consistent with the notion that greenness is water- and heat-sensitive at this site. Greenness increases with wetter years (PR; monotonic ↑) and decreases with brighter years (SRAD; monotonic ↓). Climatic water deficit (DEF) shows a convex shape, little change at low anomalies, gains toward moderate moisture availability, then a decline at the driest end, indicating sensitivity under extreme dryness. Both temperature terms are adverse overall: TMIN is decreasing strongly, and TMAX exhibits a U-shape with a trough near minor positive anomalies, implying penalties from warm nights and from very hot days. VAP declines (higher moisture associated with slightly lower greenness in these standardized units), whereas VPD exhibits a peaked response (improvements from low to moderate VPD, then losses at higher dryness). Wind speed (VS) shows a shallow, weakly U-shaped response.

To provide additional context for the climate–productivity relationships, annual growing-season climate anomalies were also summarised at the mangrove-domain scale for 2001–2023 (Figure S4 & S5). The supplementary analysis shows that climatically anomalous years were characterised by varying combinations of moisture, radiation, temperature, and atmospheric-demand anomalies rather than by a single persistent dry-condition signal. This supports a cautious interpretation of the NPP response curves: the positive response to shortwave radiation, vapour-pressure deficit, and climatic water deficit within part of the observed range should be interpreted as a context-dependent response under specific anomalous years, rather than as evidence that drier conditions are uniformly favourable for mangrove productivity.

Patterns indicate more substantial energy limitation. Modelled NPP increases sharply with SRAD (strong monotonic ↑) and, within the observed range, rises with VPD and DEF (positive, concave responses), suggesting productivity gains in brighter, drier-air years until very high moisture deficits (Fig. 10). Precipitation (PR) is weakly non-linear with a shallow trough near average conditions. Both temperature terms are predominantly negative (especially TMAX), indicating heat stress on productivity. Vapour pressure (VAP) shows a U-shape with a minimum near average anomalies, and 10 m wind speed (VS) is mildly negative to flat. Together, these responses complement the disturbance-risk analysis: years that were brighter and relatively dry tended to (i) heighten disturbance odds and (ii) depress canopy greenness (kNDVI), while NPP appeared more energy-limited, benefitting from light and (up to a point) dry-air conditions but penalized by heat. Axes in the partial plots are in SD units (x: climate anomaly; y: centered smooth effect), so shapes emphasize direction and non-linearity rather than absolute magnitudes.

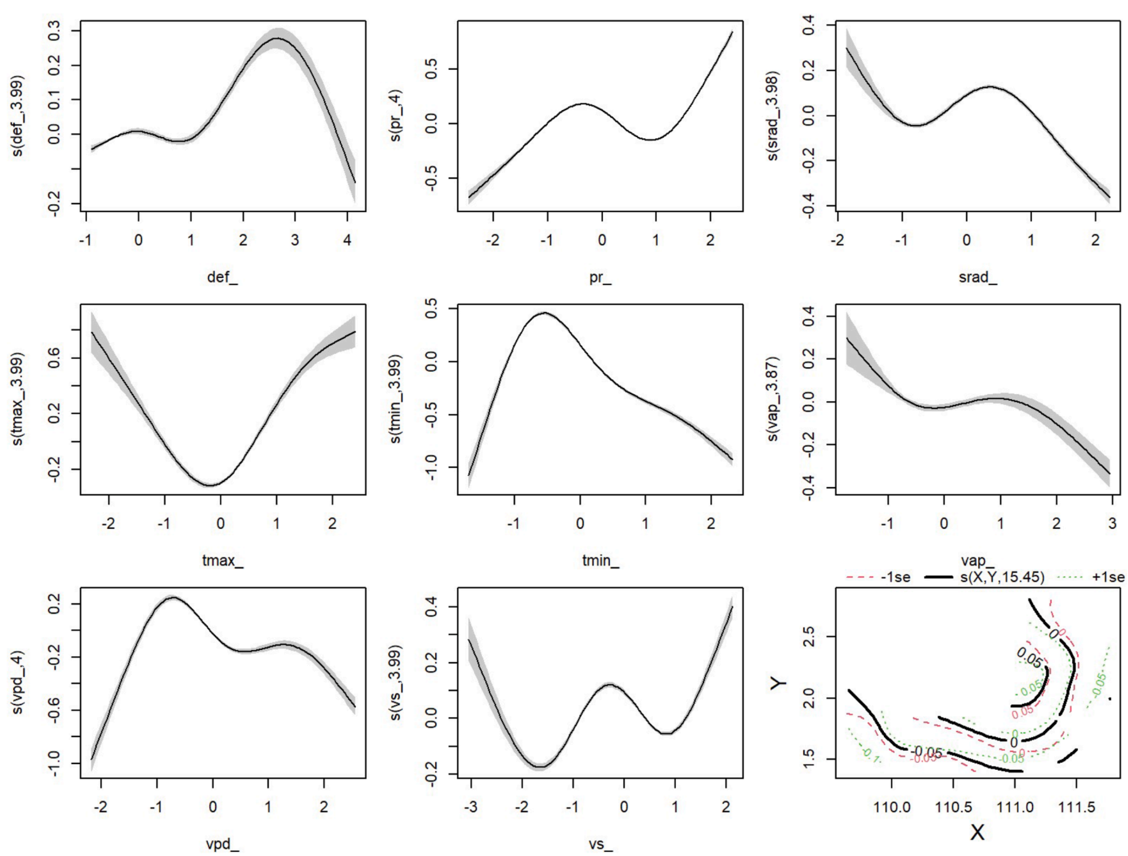

Fig. 9. Climate–productivity response of canopy greenness (GAM partial effects). Partial effects from the spatial GAM fitted to annual kNDVI anomalies (2001–2023; mangrove mask). Each panel shows the smooth term for one standardised climate anomaly (z-score; x-axis in SD units) and its centred partial effect on the fitted kNDVI anomaly (y-axis), with shaded ±2 SE ribbons. Climate covariates are: climatic water deficit (DEF), precipitation (PR), shortwave radiation (SRAD), maximum temperature (TMAX), minimum temperature (TMIN), vapour pressure (VAP), vapour pressure deficit (VPD), and wind speed (VS). Panel headers follow mgcv notation, where the trailing value denotes the effective degrees of freedom (edf) of the smooth. The bottom-right panel shows the fitted spatial smooth s(x,y), representing residual spatial structure not explained by the climate covariates.

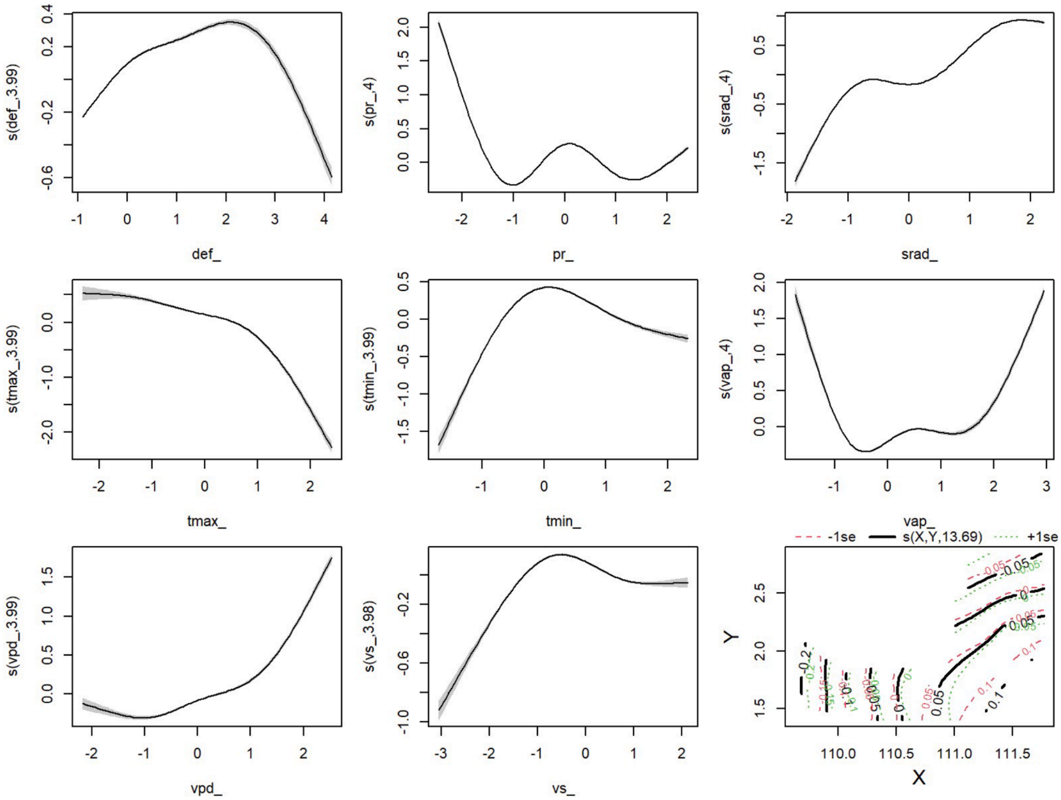

Fig. 10. Climate–productivity response of modelled net primary production. As mentioned above, the GAM was fitted to annual NPP anomalies (2001–2023). Smoothed lines depict non-linear effects of standardized climate anomalies; ribbons are ±2 SE. The spatial smooth $s(x, y)$is shown bottom-right.

3.5. *Spatial dominance of climate controls on productivity*

Dominance maps identify the climate variable with the most considerable absolute effect (|β|) at each pixel and the direction of that effect (Fig. 11). For kNDVI, minimum temperature (TMIN) is the most frequent dominant control (24.4% of mangrove area; 271.1 km^2), followed by shortwave radiation (SRAD; 14.5%; 160.6 km^2) and vapour-pressure deficit (VPD; 13.7%; 151.8 km^2) (Table S8). Dominant-sign maps indicate that the prevailing kNDVI response is negative (68.6% of area), consistent with greenness losses under cooler nights, brighter years, and higher atmospheric dryness (Table S10). The combined code map (sign × index) shows that the single largest kNDVI category is negative TMIN (code −5; 232.7 km^2), followed by negative VPD (−7; 122.0 km^2) and negative SRAD (−3; 93.7 km^2) (Table S12). In contrast, NPP is overwhelmingly energy-limited spatially, with SRAD dominating 69.3% of the mangrove area (694.5 km^2), followed by TMIN at 12.0% (120.1 km^2) (Table S9). The dominant sign is positive for 90.5% of the area (Table S11), and the single largest category is positive SRAD (+3; 691.8 km^2) (Table S13). Together, these patterns echo the GAM partials: greenness is broadly sensitive to dry/bright/cool-night stress, whereas NPP increases with light and warmer nights across most mangroves, but declines with heat extremes elsewhere.

3.6. *Vulnerability of mangrove canopy greenness and productivity to interannual climate forcing*

Greenness vulnerability v_i, is low to moderate on averag (mean = 0.28; median = 0.27; Table S17), with a distinctly right-skewed distribution. Most canopy falls below 0.4 (82.3%: 0–0.2 = 28.2%; 0.2–0.4 = 54.1%), while only 1.8% exceeds 0.6 and 0.1% exceeds 0.8 (Table S14: Fig. 12A-B). The quantile view corroborates a long, thin upper tail: each lower quartile contributes ~25%, whereas the upper decile alone accounts for ~10% of the area (Table S15). Spatial attribution clarifies the climatic pathways of sensitivity: pixels where TMIN dominates the kNDVI response occupy the largest share (271.1 km^2), followed by SRAD (160.6 km^2) and VPD (151.8 km^2) (Table S16). Taken together, these results indicate that most mangrove canopy exhibits low-to-moderate greenness vulnerability, while a comparatively small fraction of the domain concentrates higher vulnerability values and is spatially associated with areas where TMIN-, SRAD-, and VPD-linked responses dominate (Tables S14–S16; Fig. 12A–B).

By contrast, NPP vulnerability is higher and centered in the mid-range of the 0–1 scaled vulnerability index, with a mean of 0.470 and a median of 0.483 (Table S21). Class totals peak at 0.4–0.6 (59.4%), with a further 14.0% at 0.6–0.8; very low (<0.2) and very high (≥0.8) classes are rare (3.5% and 0.3%, respectively) (Table S18: Fig. 12C-D). Quantiles are near-uniform through the median (~25% each) but then concentrate into the upper tail (Q75–Q90: 15.0%; Q90–Q100: 10.0%) (Table S19). SRAD dominates the NPP response across most of the footprint (694.5 km^2), with TMIN contributing the second-largest share (120.1 km^2) (Table S20). This contrast with greenness indicates partial decoupling between canopy structure and carbon flux under year-to-year forcing. Foliage density remains comparatively buffered, while productivity responds more elastically to interannual energy variation, particularly under clear-sky, high-irradiance summers that also elevate atmospheric demand. The joint picture is therefore one of widespread structural stability with localized sensitivity to greenness, overlaid by a basin-wide propensity for NPP fluctuations driven by radiation, an attribution that helps explain why productivity “moves” more than the canopy and highlights where monitoring should prioritize combined SRAD–VPD extremes. Classified versions of the vulnerability analysis, including quantile bins and equal-width bins, are provided in the Supplementary Figure S3 A–B for kNDVI and S3 C–D for NPP, complementing Fig. 12 with cartography suited to area accounting and cross-metric comparison.

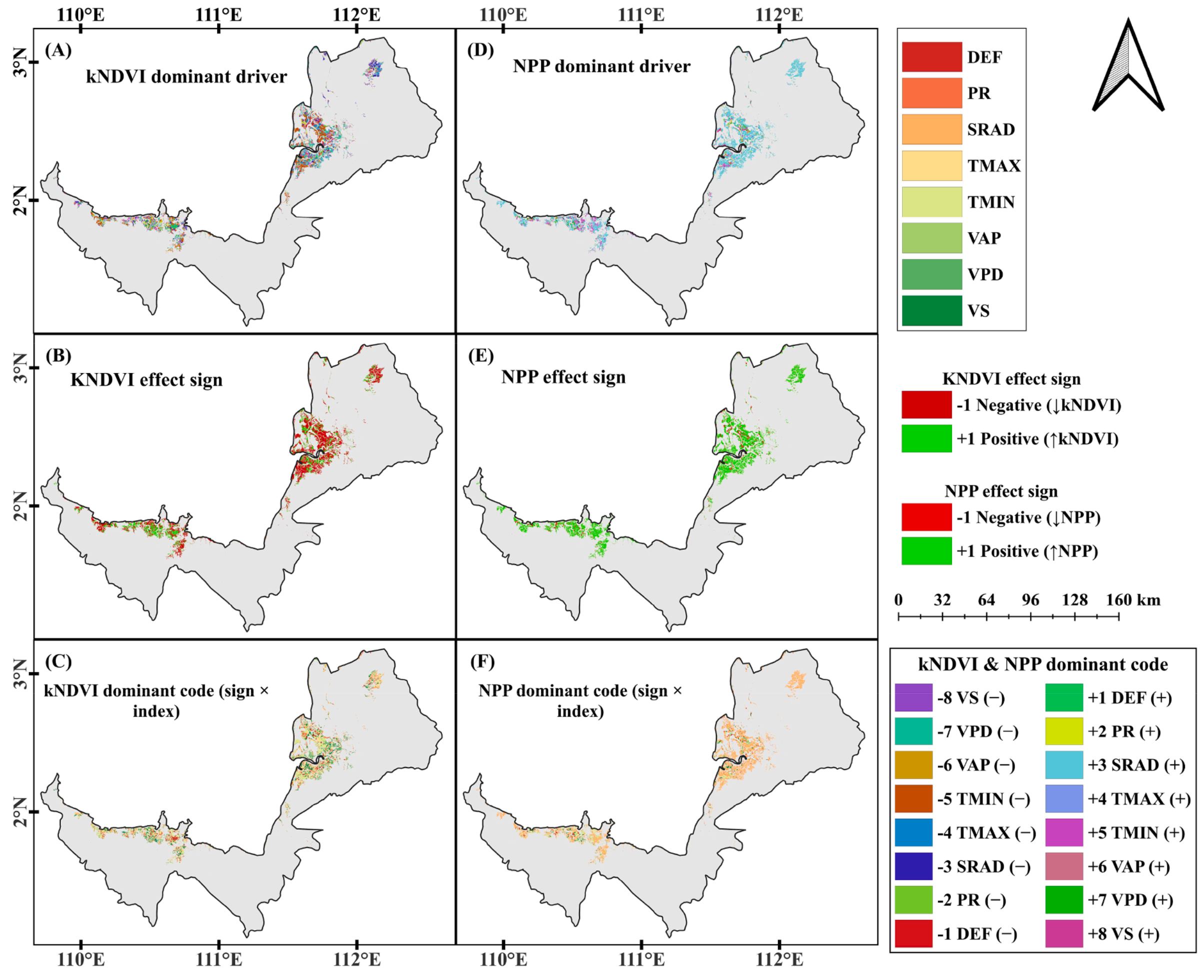

Fig. 11. Spatial dominance and effect sign of climatic controls on canopy greenness (kNDVI) and productivity (NPP). (A, D) Dominant driver per pixel, defined as the covariate with the most considerable absolute ridge elasticity $|\beta|$. (B, E) Effect sign (green = positive, red = negative): Non-mangrove is masked; all panels share the LandTrendr analysis grid. Patterns accord with the GAM partials.

3.7. Uncertainty quantification and spatial robustness

Uncertainty was quantified and spatial robustness evaluated through three complementary steps: (i) 5-fold spatial block cross-validation (~10 km blocks) to assess predictive skill; (ii) pixel-level sign-certainty and dominance-certainty diagnostics derived from the ridge elasticities to identify directionally reliable and dominant drivers; and (iii) construction of a high-certainty vulnerability index (harm-direction aggregation) normalized to [0,1]. Held-out performance indicated $RMSE/R^2$ *of* 0.93/0.10 for kNDVI and 0.76/0.40 for NPP, with near-ideal calibration (Table S21-S22). After applying a strict sign-certainty threshold (≥ 0.975), spatial patterns were coherent: for kNDVI, confidently harmful responses were led by TMIN (13.1% of the mangrove domain), while confidently protective responses were largest for TMAX (16.1%); for NPP, confidently harmful responses were dominated by SRAD (44.5%), and protective responses were led by TMIN (6.5%). Full per-driver shares and areas are reported in (Tables S23–S24). Dominant-driver labels were restricted to dominance certainty ≥ 0.95; as intended, extents are small but robust. SRAD dominates NPP over 2.81% (≈ 31.3 km^2), whereas TMIN is the leading dominant class for kNDVI but covers $<$ 0.2% (≈ 1.6 km^2). Distributions of dominance are summarized in Table S25. The high-certainty vulnerability index shows a heavier upper tail for NPP than kNDVI: exceedance areas at the q95 threshold are ≈ 55.6 km^2 (kNDVI) and ≈ 50.1 km^2 (NPP), and only ~ 0.1% of area attains ≥ 0.70 in either case (Table S26). Taken together, these diagnostics indicate stronger energy-limitation sensitivity in productivity (SRAD/TMIN signals) and mixed energy–water controls in greenness (Fig. 13).

4. Discussion

4.1. Temporal patterns and disturbance characteristics

LandTrendr ridge modelling indicates that mangrove disturbance in Sarawak accelerated after 2010, with abrupt increases in both disturbed area and patch density. Disturbances were typically minor (~1–3 ha) and spatially diffuse and, together with the strong accessibility gradients reported in the covariate analysis (e.g., proximity to roads), are consistent with localised, access-mediated disturbance and/or land-use pressures; however, the present analysis does not allow definitive attribution of individual events to specific causes (Section 3.1). Large tropical-cyclone-scale disturbances are uncommon at these latitudes**,** but non-cyclone wind events, hydrological/geomorphic change, and local conversion processes may all contribute to the observed disturbance signal. It is important to distinguish association from **cause** in our modelling results. The dominant-driver map identifies the covariate group with the largest contribution to the fitted disturbance log-odds and should not be interpreted as causal attribution. kNDVI and NPP anomalies are proximate canopy-condition proxies that integrate multiple stressors around the time of change; thus, their predictive strength reflects canopy sensitivity rather than implying that productivity "drives" disturbance. Time-since-disturbance maps indicated that ~6.8 % of the mangrove area had been disturbed in the seven years preceding

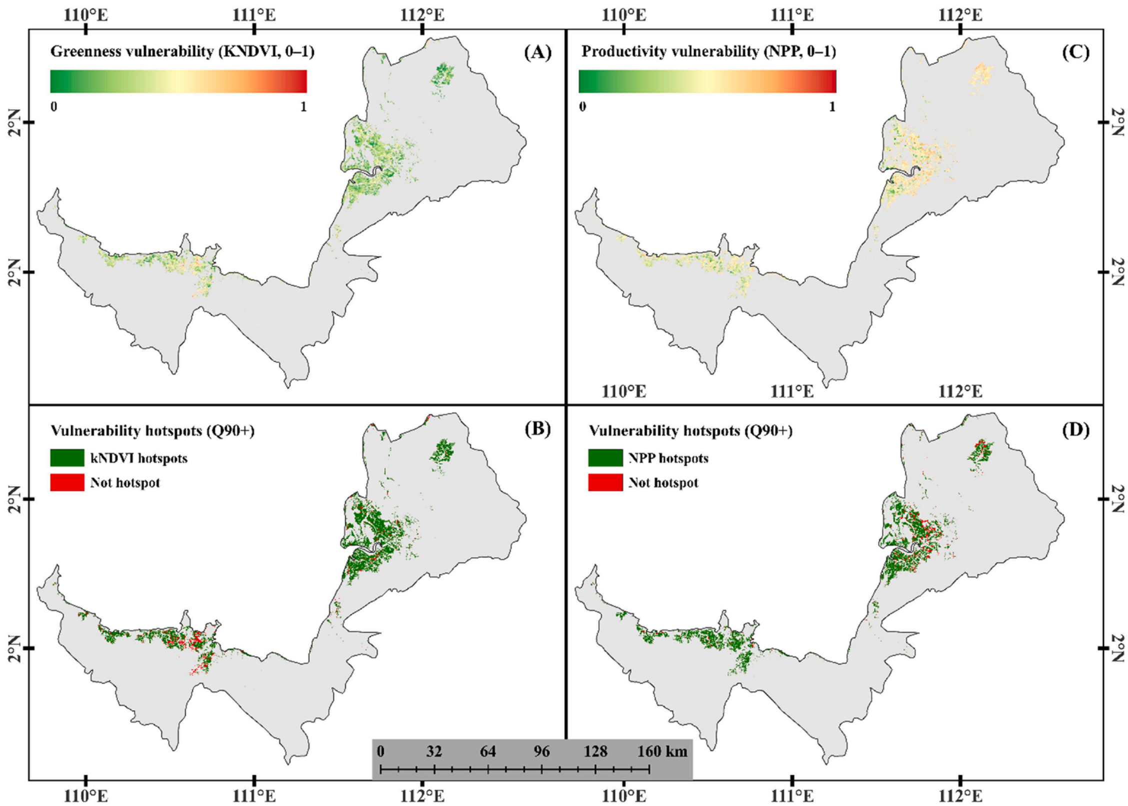

Fig. 12. Climate-driven vulnerability of mangrove canopy greenness and productivity and corresponding hotspots. (A) Greenness vulnerability (kNDVI, 0–1) and (C) productivity vulnerability (NPP, 0–1), where higher values indicate greater sensitivity to interannual climate forcing; non-mangrove areas are masked (dark background). (B, D) Q90 hotspots derived from the respective continuous surfaces: green pixels mark the top decile within the mangrove mask, red pixels denote non-hotspot mangrove pixels. The color ramp for (A, C) runs from low (0, green) to high (1, red). All panels share a common extent, projection (WGS 84 geographic), and scale bar.

2020. Such fragmentation resembles the pattern of protracted cumulative loss observed in global change analyses. Thomas et al. (2017) reported that anthropogenic activity affected 37.8% of radar/Landsat tiles globally from 1996 to 2010 and that conversion of mangroves to aquaculture/agriculture was the most frequent cause (11.2% of tiles), with Southeast Asia comprising nearly half of these occurrences. This regional concentration of small-patch losses is consistent with our finding of numerous minor disturbances in Sarawak. However, our dominance analysis does not attribute causes; it summarises which covariate group contributes most to the fitted disturbance probability for disturbed pixels. In this sense, productivity/greenness anomalies account for the largest share of dominant contributions (approximately half of disturbed pixels), indicating that canopy-condition signals around the event year are strongly informative of where disturbance is detected. These anomalies are best interpreted as proximate canopy responses that may arise from multiple pathways, including access-mediated conversion as well as climate and resource variability, rather than as evidence that "productivity causes" disturbance (Sippo et al., 2018).

4.2. Climate and productivity drivers

The logistic regression identified four climatic anomalies, precipitation, shortwave radiation (SRAD), vapour pressure deficit (VPD), and minimum temperature, as significant predictors of disturbance probability. Drier and brighter conditions (positive precipitation anomaly implying drier months and high SRAD anomaly) markedly increased disturbance odds (odds ratios ~1.23 and 1.48 respectively), whereas cooler night-time temperatures reduced odds (Table S6b). Disturbances were also more likely when net primary productivity (NPP) anomalies were positive (OR≈1.31), but greenness anomalies were negative (OR≈0.097) (Zinnert et al., 2021). These patterns can be interpreted through the lens of mangrove ecophysiology.

In tropical mangroves, the wet season supports canopy development and productivity, whereas the dry season brings physiological stress. A flux study in an eastern Amazon mangrove showed that NDVI declined from ~0.75 in the wet season to ~0.69 in the dry season; during dry periods, high incident radiation coupled with reduced precipitation led to leaf abscission and declines in leaf area index (Freire et al., 2022). Photosynthesis and respiration peaks occurred in the wet season due to high rainfall and cloudiness, which lowered radiation stress (Asbridge et al., 2018). Our finding that positive SRAD anomalies increase disturbance probability aligns with this energy-limited scenario; excessive radiation exacerbates drought stress and can induce defoliation, making stands more detectable by LandTrendr.

Rainfall exerts a dominant influence on mangrove phenology and productivity. A phenology study in southern Thailand concluded that high rainfall increased mangrove growth, while decreased rainfall led to increased salinity and reduced net productivity (Songsom et al., 2019). In this study, positive precipitation anomalies (indicating a preceding dry period) were associated with higher odds of disturbance, suggesting that water stress triggers leaf loss or dieback, which LandTrendr misclassifies as disturbance. The adverse effect of cooler night-time temperature anomalies mirrors observations from subtropical mangrove carbon flux studies, where warmer nocturnal temperatures drove respiration rates above 4 μmol CO_2 m^{-2} s^{-1} (Raw et al., 2023); cooler nights suppress respiration and thus may buffer the canopy against carbon imbalance and leaf senescence.

The strong positive effect of NPP anomalies, yet the adverse effect of greenness anomalies, might appear counterintuitive, but it underscores

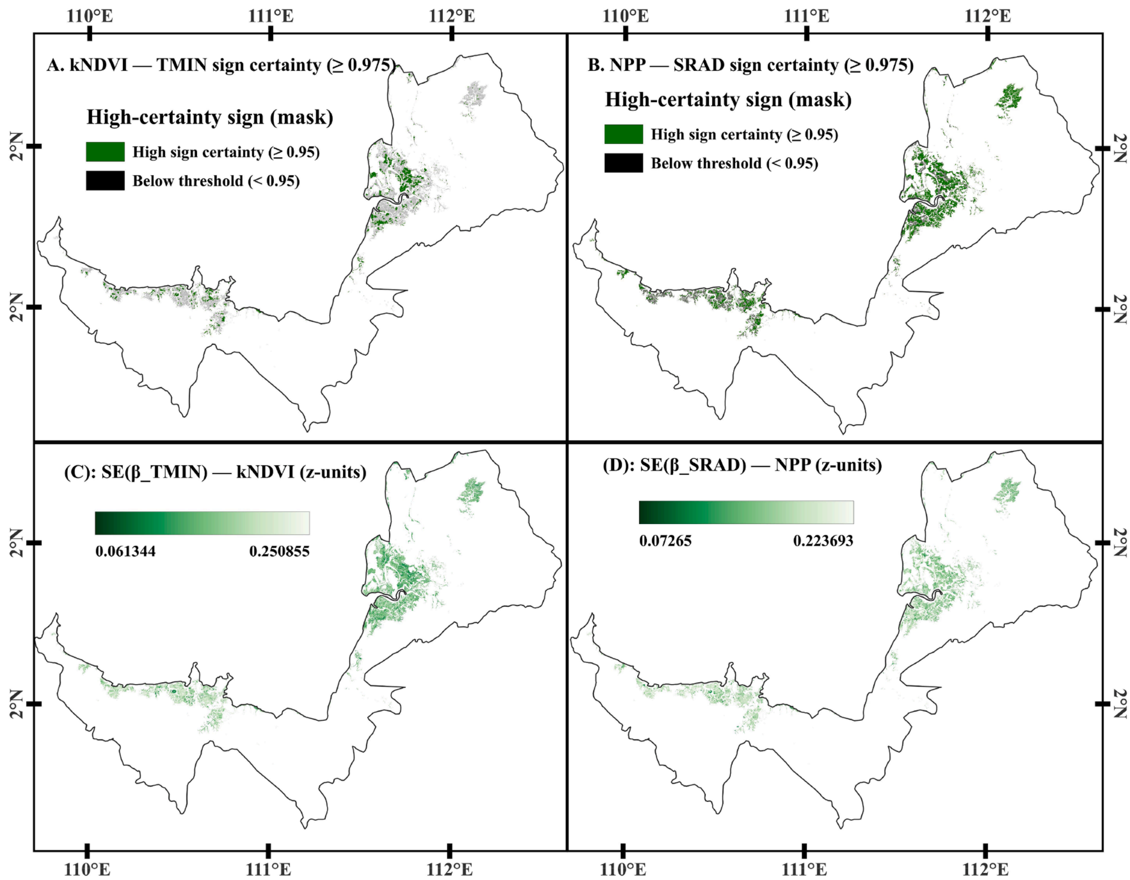

Fig. 13. Uncertainty diagnostics for climate–productivity responses. (A) Binary mask of TMIN→ kNDVI sign certainty at ≥ 0.95**;** (B) binary mask of SRAD→NPP sign certainty at ≥ **0.975**; (C) coefficient standard error SE(β_TMIN) for kNDVI (z-units); (D) SE(β_SRAD) for NPP (z-units). Masks show where the effect direction is estimated with high confidence; standard-error maps summarize parameter precision.

the decoupling between photosynthetic carbon assimilation and canopy greenness under stress (Gandhi and Jones, 2019). High NPP anomalies may reflect short bursts of productivity following nutrient pulses (e.g., monsoonal flooding), which can be accompanied by subsequent leaf turnover. Greenness anomalies, on the other hand, capture the structural canopy state. Globally, precipitation is the dominant driver of interannual variability in plant productivity (Adame et al., 2021), and our results reinforce that water-availability anomalies modulate mangrove NPP. However, SRAD explained the largest share of productivity variance in our ridge regression, indicating an energy-limited system where radiant energy, rather than water, constrains productivity for much of the year (Thomas et al., 2017). This explains why high SRAD anomalies are associated with disturbance: sudden increases in radiation may exceed the photosynthetic optimum, inducing photoinhibition and canopy stress. The dominance of SRAD in the NPP vulnerability surfaces is consistent with an energy-limited signal in which interannual variation in incoming radiation exerts a strong constraint on carbon uptake, even where canopy greenness remains comparatively buffered. This pattern implies a partial decoupling between canopy structural condition (kNDVI) and carbon flux (NPP) under year-to-year forcing, and it motivates monitoring that jointly considers radiation and atmospheric-demand extremes (e.g., SRAD–VPD co-occurrence) when anticipating productivity downturns.

4.3. Anthropogenic drivers and their interactions

Among anthropogenic covariates, road distance exerted the most substantial effect: sites closer to roads had substantially higher odds of disturbance (OR≈0.29 per SD increase), whereas built-up intensity was not significant. Distances to water and to mangrove edges also showed positive associations with disturbance, indicating that accessibility from waterways and edges facilitates human entry. These findings align with global patterns, where infrastructure expansion often underpins mangrove deforestation. The Food and Agriculture Organization estimates that aquaculture development drove 27 % of global mangrove loss between 2000 and 2020, while natural retraction accounted for 26 %; oil palm and rice cultivation each contributed about 8 % (FAO, 2023). Southeast Asia, where most of Sarawak's mangroves occur, experienced ~68 % of global loss during 2000–2010 and ~54 % during 2010–2020 (Mitra et al., 2023). Thomas et al. (2017) showed that anthropogenic conversion, mainly for aquaculture and agriculture (oil palm, rice), was the predominant cause of loss in the region. Built-up intensity was not a significant predictor, consistent with the remoteness of Sarawak's mangroves. By contrast, road corridors enable access to remote stands, facilitating the expansion of logging and aquaculture. As aquaculture booms recede, oil-palm cultivation has become a more prominent driver (Yaseen et al., 2023), which may explain the post-2010 surge in disturbance area and patch density.

The synergy between climate stress and anthropogenic activity is noteworthy. Dry periods with high SRAD anomalies not only weaken mangrove health but also coincide with low river discharge, making coastlines more accessible for fuelwood collection or clearing (Hagger et al., 2022). When high NPP anomalies attract human exploitation (for charcoal or timber), subsequent climate stress may intensify canopy loss, creating the small patches detected (Duke et al., 2017). The ridge regression indicated that climate and anthropogenic variables jointly explained ~44% of the disturbance, highlighting that socio-ecological dynamics, rather than single factors, drive mangrove degradation.

Observing similar patterns globally, Friess et al. (2019) argued that economic incentives for shrimp farming and oil-palm cultivation often outweigh long-term ecosystem service benefits, leading to high conversion rates despite existing protection measures.

4.4. Implications for management and conservation

The results call for integrated management strategies that address both climatic vulnerability and anthropogenic pressures. The dominance of productivity and greenness anomalies as immediate drivers implies that remote sensing can serve as an early warning system: detecting anomalously high SRAD or extended dry spells may help predict potential dieback events (Gerona-Daga and Salmo, 2022). Management agencies should focus on maintaining hydrological connectivity and shade to buffer mangroves against radiation stress. Conservation efforts must also prioritize access control, limit road construction, and regulate waterways to reduce human entry into vulnerable stands. The strong influence of distance to road on disturbance probability underscores the importance of spatial planning; establishing exclusion zones around core mangrove areas and promoting alternative livelihood opportunities could lessen the impetus for encroachment. Given that national-level governance alone has proven insufficient to curb mangrove loss (López-Angarita et al., 2016). Decentralized or community-based management may be better suited for Sarawak's context.

Climate change compounds these challenges. The FAO notes that climate impacts sea-level rise, rainfall variability, and increased storm severity have already tripled the area of mangroves lost to natural disasters in recent decades (Vogt et al., 2019). Our finding that climate anomalies account for roughly one-fifth of the disturbance probability suggests that adaptation measures (e.g., facilitating the inland migration of mangroves, restoring degraded edges) are essential. Protecting large contiguous mangrove tracts, which exhibited lower disturbance probability, will enhance resilience by enabling natural recovery and providing refugia (Jayanthi et al., 2023). Finally, global comparison underscores the need for international cooperation: Sarawak's trends mirror broader Southeast Asian patterns of small-patch losses driven by aquaculture, agriculture, and climate extremes (FAO and UNEP, 2020). By integrating local monitoring with global initiatives (e.g., Sustainable Development Goal 14 and the Mangrove Restoration Potential), Sarawak can contribute to reversing regional decline.

4.5. Limitations and future research

Analyses relied on Landsat-based disturbance detection and logistic models, which, despite high AUC values (~0.91), may misclassify events such as canopy thinning, natural senescence, or post-disturbance recovery as disturbances. Furthermore, the climatological anomalies were derived from coarse (0.05–0.25°) products, potentially smoothing micro-climatic variations that influence mangrove physiology. Future work should incorporate high-resolution climatic data and field measurements of salinity, nutrients, and tidal inundation to refine causal relationships. Exploring machine-learning models that account for nonlinear interactions between climate, productivity, and socioeconomic variables may improve predictive performance. Socioeconomic surveys could elucidate the motivations behind local harvesting activities and guide targeted interventions. Ultimately, longitudinal studies that link disturbance detection to subsequent regrowth will be crucial for evaluating the resilience and recovery potential of Sarawak's mangroves under a changing climate.

5. Conclusion

Since 2010, Sarawak's mangroves have undergone frequent, spatially fragmented degradation: disturbed area and patch density rose sharply, yet typical events remained small (≈1–3 ha), indicating dispersed, localised change rather than a few catastrophic clearances. This trajectory is corroborated by robust time-series metrics and sensitivity checks, with cumulative disturbed area concentrated post-2010 and sustained peaks through 2017–2023. Event-year anomalies in canopy condition emerge as the dominant proximate signal of mapped disturbance: greenness anomalies are strongly associated with lower disturbance odds, whereas positive NPP anomalies are associated with higher odds; among climate covariates, brighter and drier-than-average years correspond to higher disturbance odds, while cooler nights **appear** protective. Accessibility strongly modulates where these signals coincide with mapped disturbance, with proximity to roads showing a consistent association with higher disturbance probability, whereas built-up intensity is comparatively uninformative after accounting for distance gradients.

With respect to causes, our results support an interpretation of predominantly access-mediated, small-patch disturbance occurring in a landscape where canopy condition is sensitive to interannual climate variability; however, the analysis does not directly classify post-disturbance land use and therefore cannot quantify the fraction attributable to specific processes (e.g., conversion to aquaculture/agriculture, infrastructure expansion, or storm/geomorphic impacts). Even so, the combination of fragmented patch geometry and strong road-proximity gradients is consistent with incremental human encroachment and conversion pressures, while the climate–canopy relationships indicate that anomalously bright and dry seasons may heighten susceptibility and reduce recovery capacity in affected stands.

These findings offer an operational template for management. Priority should be given to recently disturbed sites, where edge instability and early successional stages are most likely, paired with targeted access control along roads and waterways and routine surveillance of seasonal radiation–dryness anomalies as an early-warning layer. By linking multi-decadal Landsat segmentation to event-year anomalies and spatial accessibility, this study provides a transferable framework for diagnosing where and when mangrove canopies are most vulnerable and for guiding monitoring, enforcement, and restoration planning across Sarawak and comparable deltas.

Ethics approval and consent to participate

Not Applicable.

Consent for publication

Not Applicable.

Funding

No Funding.

CRediT authorship contribution statement

Abdul Qaiyum Alidin: Writing – review & editing, Writing – original draft, Visualization, Validation, Software, Methodology, Investigation, Formal analysis, Data curation, Conceptualization. **Azlizam Aziz:** Writing – review & editing, Visualization, Data curation. **Waseem Razzaq Khan:** Writing – review & editing, Investigation, Formal analysis. **Shazali Johari:** Writing – review & editing, Supervision, Methodology, Conceptualization.

Declaration of competing interest

The authors declare no conflict of interest.

Acknowledgements

Authors acknowledge the support of the Universiti Putra Malaysia.

Supplementary materials

Supplementary material associated with this article can be found, in the online version, at doi:10.1016/j.tfp.2026.101326.

Data availability

https://github.com/skm321786/Mangrove-Degradation-and-Climate-Productivity-Drivers-in-Sarawak-Malaysian-Borneo.git

References

Abatzoglou, J.T., Dobrowski, S.Z., Parks, S.A., Hegewisch, K.C., 2018. TerraClimate, a high-resolution global dataset of monthly climate and climatic water balance from 1958-2015. Sci. Data 5. https://doi.org/10.1038/sdata.2017.191.

Adame, M.F., Connolly, R.M., Turschwell, M.P., Lovelock, C.E., Fatoyinbo, T., Lagomasino, D., Goldberg, L.A., Holdorf, J., Friess, D.A., Sasmito, S.D., Sanderman, J., Sievers, M., Buelow, C., Kauffman, J.B., Bryan-Brown, D., Brown, C. J., 2021. Future carbon emissions from global mangrove forest loss. Glob. Chang. Biol. 27, 2856–2866. https://doi.org/10.1111/gcb.15571.

Alam, M.M., Siwar, C., bin Toriman, M.E., Molla, R.I., Talib, B., 2012. Climate change induced adaptation by paddy farmers in Malaysia. Mitig. Adapt. Strateg. Glob. Chang. 17, 173–186. https://doi.org/10.1007/s11027-011-9319-5.

Anees, S.A., Mehmood, K., Khan, W.R., Sajjad, M., Alahmadi, T.A., Alharbi, S.A., Luo, M., 2024a. Integration of machine learning and remote sensing for above ground biomass estimation through Landsat-9 and field data in temperate forests of the Himalayan region. Ecol. Inf. 82, 102732. https://doi.org/10.1016/j.ecoinf.2024.102732.

Anees, S.A., Mehmood, K., Khan, W.R., Shahzad, F., Zhran, M., Ayub, R., Alarfaj, A.A., Alharbi, S.A., Liu, Q., 2025a. Spatiotemporal dynamics of vegetation cover: integrative machine learning analysis of multispectral imagery and environmental predictors. Earth Sci. Inf. 18. https://doi.org/10.1007/s12145-024-01673-0.

Anees, S.A., Mehmood, K., Luo, M., Abuelgasim, A., Pan, S.A., Shahzad, F., Muhammad, S., Khan, W.R., 2025b. Advancing forest fire burn severity and vegetation recovery assessments using remote sensing and machine learning approaches. Ecol. Inf. 92, 103446. https://doi.org/10.1016/j.ecoinf.2025.103446.

Anees, S.A., Mehmood, K., Muhammad, S., Luo, M., Shahzad, F., Khan, W.R., 2025c. Spatiotemporal dynamics and environmental drivers of fractional vegetation cover in a Semi-Arid region using machine learning. Theor. Appl. Clim. 156 (9), 1–23. https://doi.org/10.1007/s00704-025-05696-5.

Anees, S.A., Mehmood, K., Raza, S.I.H., Pfautsch, S., Shah, M., Jamjareegulgarn, P., Shahzad, F., Alarfaj, A.A., Alharbi, S.A., Khan, W.R., Dube, T., 2025d. Spatiotemporal analysis of surface urban heat island intensity and the role of vegetation in six major Pakistani cities. Ecol. Inf. 85, 102986. https://doi.org/10.1016/j.ecoinf.2024.102986.

Anees, S.A., Mehmood, K., Rehman, A., Rehman, N.U., Muhammad, S., Shahzad, F., Hussain, K., Luo, M., Alarfaj, A.A., Alharbi, S.A., Khan, W.R., 2024b. Unveiling fractional vegetation cover dynamics: a spatiotemporal analysis using MODIS NDVI and machine learning. Environ. Sustain. Indic. 24, 100485. https://doi.org/10.1016/j.indic.2024.100485.

Araya-Lopez, R., de Paula Costa, M.D., Wartman, M., Macreadie, P.I., 2023. Trends in the application of remote sensing in blue carbon science. Ecol. Evol. 13. https://doi.org/10.1002/ece3.10559.

Asbridge, E., Lucas, R., Rogers, K., Accad, A., 2018. The extent of mangrove change and potential for recovery following severe tropical cyclone Yasi, Hinchinbrook island, Queensland, Australia. Ecol. Evol. 8, 10416–10434. https://doi.org/10.1002/ece3.4485.

Bennett, M., March, A., Raguain, J., Failler, P., 2024. Blueprint for blue carbon: lessons from Seychelles for small island states. Oceans 5, 81–108. https://doi.org/10.3390/oceans5010006.

Bey, R., Goussault, R., Grolleau, F., Benchoufi, M., Porcher, R., 2020. Fold-stratified cross-validation for unbiased and privacy-preserving federated learning. J. Am. Med. Inform. Assoc. 27, 1244–1251. https://doi.org/10.1093/jamia/ocaa096.

Blanton, et al., 2024. is: ecotourism and mangrove conservation in southeast Asia: current trends and perspectives. J. Env. Manage. 365, 121529. https://doi.org/10.1016/j.jenvman.2024.121529.

Bunting, P., Hilarides, L., Rosenqvist, A., Lucas, R.M., Kuto, E., Gueye, Y., Ndiaye, L., 2023. Global Mangrove watch: monthly alerts of Mangrove loss for Africa. Remote Sens. (Basel) 15, 2050. https://doi.org/10.3390/rs15082050.

Bunting, P., Rosenqvist, A., Hilarides, L., Lucas, R.M., Thomas, N., Tadono, T., Worthington, T.A., Spalding, M., Murray, N.J., Rebelo, L.M., 2022. Global Mangrove extent change 1996–2020: global Mangrove watch version 3.0. Remote Sens. (Basel) 14, 3657. https://doi.org/10.3390/rs14153657.

Bunting, P., Rosenqvist, A., Lucas, R.M., Rebelo, L.M., Hilarides, L., Thomas, N., Hardy, A., Itoh, T., Shimada, M., Finlayson, C.M., 2018. The global mangrove watch - a new 2010 global baseline of mangrove extent. Remote Sens. (Basel) 10, 1669. https://doi.org/10.3390/rs10101669.

Dermawan, O., Aryani, W.D., Mulyasa, E., Yusuf, T.K., Yanti, R., 2024. Species composition and density in the Mangrove forest area of Sriminosari village, Labuhan Maringgaika district, east Lampung Regency. In: E3S Web of Conferences. https://doi.org/10.1051/e3sconf/202448201004.

Ding, N., Li, M., 2023. Mapping forest abrupt disturbance events in southeastern China—comparisons and tradeoffs of landsat time series analysis algorithms. Remote Sens. (Basel) 15, 5408. https://doi.org/10.3390/rs15225408.

Dong, H., Gao, Y., Chen, R., Wei, L., 2024. MangroveSeg: deep-supervision-guided feature aggregation network for Mangrove detection and segmentation in satellite images. Forests 15, 127. https://doi.org/10.3390/f15010127.

Duke, N.C., Kovacs, J.M., Griffiths, A.D., Preece, L., Hill, D.J.E., Van Oosterzee, P., Mackenzie, J., Morning, H.S., Burrows, D., 2017. Large-scale dieback of mangroves in Australia's Gulf of Carpentaria: a severe ecosystem response, coincidental with an unusually extreme weather event. Mar. Freshw. Res. 68, 1816–1829. https://doi.org/10.1071/MF16322.

FAO, UNEP, 2020. The State of World's Forests 2020. Forests, Biodiversity and People, Geographical Review.

FAO, 2023. The World's Mangroves 2000–2020. Food and Agriculture Organization of the United Nations, Rome, p. 63. https://doi.org/10.4060/cc7044e.

Freire, A.S.C., Vitorino, M.I., de Souza, A.M.L., Germano, M.F., 2022. Analysis of the energy balance and CO2 flow under the influence of the seasonality of climatic elements in a mangrove ecosystem in eastern Amazon. Int. J. Biometeorol. 66, 647–659. https://doi.org/10.1007/s00484-021-02224-8.

Friess, D.A., Rogers, K., Lovelock, C.E., Krauss, K.W., Hamilton, S.E., Lee, S.Y., Lucas, R., Primavera, J., Rajkaran, A., Shi, S., 2019. The state of the world's mangrove forests: past, present, and future. Annu Rev Env. Resour. 44, 89–115. https://doi.org/10.1146/annurev-environ-101718-033302.

Gandhi, S., Jones, T.G., 2019. Identifying mangrove deforestation hotspots in south Asia, southeast Asia and Asia-Pacific. Remote Sens. (Basel) 11, 728. https://doi.org/10.3390/RS11060728.

Gelabert, P.J., Rodrigues, M., de la Riva, J., Ameztegui, A., Sebastià, M.T., Vega-Garcia, C., 2021. LandTrendr smoothed spectral profiles enhance woody encroachment monitoring. Remote Sens. Env. 262, 112521. https://doi.org/10.1016/j.rse.2021.112521.

Gerona-Daga, M.E.B., Salmo, S.G., 2022. A systematic review of mangrove restoration studies in Southeast Asia: challenges and opportunities for the United Nation's decade on ecosystem restoration. Front. Mar. Sci. 9. https://doi.org/10.3389/fmars.2022.987737.

Ghosh, S., Proisy, C., Muthusankar, G., Hassenrück, C., Helfer, V., Mathevet, R., Andrieu, J., Balachandran, N., Narendran, R., 2022. Multiscale diagnosis of mangrove status in data-poor context using very high spatial resolution satellite images: a case study in Pichavaram Mangrove forest, Tamil Nadu, India. Remote Sens. (Basel) 14, 2317. https://doi.org/10.3390/rs14102317.

Gou, R., Feng, J., Zhou, H., Lang, T., Zhao, J., Mo, L., Song, S., Lin, G., 2024. CO2 fluxes contrast between aquaculture ponds and mangrove forests and its implications for coastal wetland rehabilitation in Leizhou Peninsula, China. Agric Ecosyst Env. 367, 108968. https://doi.org/10.1016/j.agee.2024.108968.

Hagger, V., Worthington, T.A., Lovelock, C.E., Adame, M.F., Amano, T., Brown, B.M., Friess, D.A., Landis, E., Mumby, P.J., Morrison, T.H., O'Brien, K.R., Wilson, K.A., Zganjar, C., Saunders, M.I., 2022. Drivers of global mangrove loss and gain in social-ecological systems. Nat. Commun. 13. https://doi.org/10.1038/s41467-022-33962-x.

Hu, Z., Wu, J., Wang, J., Zhang, Y., Zhou, H., Gao, C., Wang, J., Wu, G., 2023. How exotic Sonneratia species affect the spatiotemporal dynamics of mangroves in Shenzhen Bay, China: a remote sensing perspective. Ecol. Indic. 153, 110479. https://doi.org/10.1016/j.ecolind.2023.110479.

Husna, J., Wijayanti, I., Budiastusi Wiratmo, L., Indrahti, S., Naryoso, A., Edzan Che Nasir, N., Patria Ratna, M., Mulyaning Andini, B., Raihan Putra Ratarno, D., 2023. Mapping the scientific literature on mangrove conservation in Indonesia: a bibliometric analysis to environmental research. In: E3S Web of Conferences. https://doi.org/10.1051/e3sconf/202344803036.

Jayanthi, M., Duraisamy, M., Kabiraj, S., Thirumurthy, S., Samynathan, M., Panigrahi, A., Muralidhar, M., 2023. Are the Sundarbans, the World's largest mangroves region under threat?—An ecosystem-based geospatial approach to assess changes past, present, and future in relation to natural and human-induced factors. Land. Degrad. Dev. 34, 125–141. https://doi.org/10.1002/ldr.4448.

Kennedy, R.E., Yang, Z., Cohen, W.B., 2010. Detecting trends in forest disturbance and recovery using yearly Landsat time series: 1. LandTrendr - temporal segmentation algorithms. Remote Sens. Env. 114, 2897–2910. https://doi.org/10.1016/j.rse.2010.07.008.

Kennedy, R.E., Yang, Z., Gorelick, N., Braaten, J., Cavalcante, L., Cohen, W.B., Healey, S., 2018. Implementation of the LandTrendr algorithm on Google Earth engine. Remote Sens. (Basel) 10, 691. https://doi.org/10.3390/rs10050691.

Khan, W.R., Giani, M., Bevilacqua, S., Anees, S.A., Mehmood, K., Nazre, M., Haddy, A.A. B.A., Median, A.N.B.A., Bujang, J.B., Mohamad-Ismail, F.N., Mohamed, J., 2025. Derivation of allometric equations and carbon content estimation in mangrove forests of Malaysia. Environ. Sustain. Indic. 26, 100618.

Khan, W.R., Nazre, M., Akram, S., Anees, S.A., Mehmood, K., Ibrahim, F.H., Zhu, X., 2024. Assessing the productivity of the Matang Mangrove forest reserve: review of one of the best-managed Mangrove forests. Forests 15 (5), 747. https://doi.org/10.3390/f15050747.

Lestari, S.D., Leon, F.M., Riyadi, S., Qodariah, Putra, A.H.P.K., 2024. Comparison and implementation of environmental law policies in handling climate change in ASEAN countries: a comparative study of Indonesia, Malaysia, and Thailand. Int. J. Energy Econ. Policy 14, 687–700. https://doi.org/10.32479/ijeep.14998.

Li, P., Jiang, L., Feng, Z., 2013. Cross-comparison of vegetation indices derived from landsat-7 enhanced thematic mapper plus (ETM+) and landsat-8 operational land imager (OLI) sensors. Remote Sens. (Basel) 6, 310–329. https://doi.org/10.3390/rs6010310.

Liu, Q., Liu, L., Zhang, Y., Wang, Z., Guo, R., 2023. Seasonal fluctuations of marsh wetlands in the headwaters of the Brahmaputra, Ganges, and Indus Rivers, Tibetan plateau based on the adapted LandTrendr model. Ecol. Indic. 152, 110360. https://doi.org/10.1016/j.ecolind.2023.110360.

López-Angarita, J., Roberts, C.M., Tilley, A., Hawkins, J.P., Cooke, R.G., 2016. Mangroves and people: lessons from a history of use and abuse in four Latin American countries. For. Ecol. Manage. 368, 151–162. https://doi.org/10.1016/j.foreco.2016.03.020.

Mehmood, K., Anees, S.A., Luo, M., Akram, M., Zubair, M., Khan, K.A., Khan, W.R., 2024a. Assessing Chilgoza Pine (Pinus gerardiana) forest fire severity: remote sensing analysis, correlations, and predictive modeling for enhanced management strategies. Trees For. People 16, 100521. https://doi.org/10.1016/j.tfp.2024.100521.

Mehmood, K., Anees, S.A., Muhammad, S., Albasher, G., Shahzad, F., Hussain, K., Liu, Q., Ayub, R., Khan, W.R., 2025a. Spatial and temporal vegetation dynamics from 2000 to 2023 in the western Himalayan regions. Stoch. Environ. Res. Risk Assess. 39, 2309–2330. https://doi.org/10.1007/s00477-025-02971-9.

Mehmood, K., Anees, S.A., Muhammad, S., Hussain, K., Shahzad, F., Liu, Q., Ansari, M.J., Alharbi, S.A., Khan, W.R., 2024b. Analyzing vegetation health dynamics across seasons and regions through NDVI and climatic variables. Sci. Rep. 14 (1), 11775. https://doi.org/10.1038/s41598-024-62464-7.

Mehmood, K., Anees, S.A., Muhammad, S., Shahzad, F., Liu, Q., Khan, W.R., Shrahili, M., Ansari, M.J., Dube, T., 2025b. Machine learning and spatio temporal analysis for assessing ecological impacts of the billion tree afforestation project. Ecol. Evol. 15, e70736.

Mehmood, K., Anees, S.A., Rehman, A., Rehman, N.U., Muhammad, S., Shahzad, F., Liu, Q., Alharbi, S.A., Alfarraj, S., Ansari, M.J., Khan, W.R., 2024c. Assessment of climatic influences on net primary productivity along elevation gradients in temperate ecoregions. Trees For. People 18, 100657.

Mehmood, K., Anees, S.A., Shahzad, F., Muhammad, S., Liu, Q., Khan, W.R., Shah, M., Jamjareegulgarn, P., 2025c. Exploring vegetation health in southern Thailand under climate stress from temperature and water impacts between 2000 and 2023. Sci. Rep. 15 (1), 30491. https://doi.org/10.1038/s41598-025-16293-x.

Mihi, A., Ghazela, R., wissal, D., 2022. Mapping potential desertification-prone areas in North-Eastern Algeria using logistic regression model, GIS, and remote sensing techniques. Env. Earth Sci. 81. https://doi.org/10.1007/s12665-022-10513-7.

Mitra, S., Roy Chowdhury, R., Saha, A., Mukherjee, K., Bhadra, T., 2023. GIS-based valuation of ecosystem services in the lower Delta Plain of West Bengal with special reference to Indian Sundarbans. In: IOP Conference Series: Earth and Environmental Science. https://doi.org/10.1088/1755-1315/1164/1/012004.

Mugiraneza, T., Nascetti, A., Ban, Y., 2020. Continuous monitoring of urban land cover change trajectories with landsat time series and landtrendr-google earth engine cloud computing. Remote Sens. (Basel) 12, 2883. https://doi.org/10.3390/RS12182883.

Pasquarella, V.J., Arévalo, P., Bratley, K.H., Bullock, E.L., Gorelick, N., Yang, Z., Kennedy, R.E., 2022. Demystifying LandTrendr and CCDC temporal segmentation. Int. J. Appl. Earth Obs. Geoinf. 110, 102806. https://doi.org/10.1016/j.jag.2022.102806.

Pérez, C.C., Olthoff, A.E., Hernández-Trejo, H., Rullán-Silva, C.D., 2022. Evaluating the best spectral indices for burned areas in the tropical Pantanos de Centla biosphere reserve, southeastern Mexico. Remote Sens. Appl. 25, 100664. https://doi.org/10.1016/j.rsase.2021.100664.

Qiu, D., Liang, Y., Shang, R., Chen, J.M., 2023. Improving LandTrendr forest disturbance mapping in China using multi-season observations and multispectral indices. Remote Sens. (Basel) 15, 2381. https://doi.org/10.3390/rs15092381.

Raw, J.L., Van der Stocken, T., Carroll, D., Harris, L.R., Rajkaran, A., Van Niekerk, L., Adams, J.B., 2023. Dispersal and coastal geomorphology limit potential for mangrove range expansion under climate change. J. Ecol. 111, 139–155. https://doi.org/10.1111/1365-2745.14020.

Schürholz, D., Castellanos-Galindo, G.A., Casella, E., Mejía-Rentería, J.C., Chennu, A., 2023. Seeing the forest for the trees: mapping cover and counting trees from aerial images of a mangrove forest using artificial intelligence. Remote Sens. (Basel) 15, 3334. https://doi.org/10.3390/rs15133334.

Shahzad, F., Mehmood, K., Anees, S.A., Adnan, M., Hussain, K., Khan, W.R., Shah, M., Jamjareegulgarn, P., Oliveira, M., Borges, J.G., 2025a. Understanding green house gases emission dynamics from forest fires in Thailand using predictive models. Glob. Planet. Change, 105236.

Shahzad, F., Mehmood, K., Anees, S.A., Adnan, M., Muhammad, S., Haidar, I., Ali, J., Hussain, K., Feng, Z., Khan, W.R., 2025b. Advancing forest fire prediction: a multi-layer stacking ensemble model approach. Earth Sci. Inf. 18 (3), 270. https://doi.org/10.1007/s12145-025-01782-4.

Singgalen, Y.A., 2022. Tourism infrastructure development and transformation of vegetation index in Dodola island of Morotai island regency. J. Inf. Syst. Inform. 4 (1), 130–144.

Sippo, J.Z., Lovelock, C.E., Santos, I.R., Sanders, C.J., Maher, D.T., 2018. Mangrove mortality in a changing climate: an overview. Estuar. Coast. Shelf. Sci. 215, 241–249. https://doi.org/10.1016/j.ecss.2018.10.011.

Songsom, V., Koedsin, W., Ritchie, R.J., Huete, A., 2019. Mangrove phenology and environmental drivers derived from remote sensing in southern Thailand. Remote Sens. (Basel) 11, 955. https://doi.org/10.3390/rs11080955.

Sun, Z., Jiang, W., Ling, Z., Zhong, S., Zhang, Z., Song, J., Xiao, Z., 2023. Using multisource high-resolution remote sensing data (2 m) with a habitat–tide–semantic segmentation approach for mangrove mapping. Remote Sens. (Basel) 15, 5271. https://doi.org/10.3390/rs15225271.

Szeghalmy, S., Fazekas, A., 2023. A comparative study of the use of stratified cross-validation and distribution-balanced stratified cross-validation in imbalanced learning. Sensors 23, 2333. https://doi.org/10.3390/s23042333.

Thomas, N., Lucas, R., Bunting, P., Hardy, A., Rosenqvist, A., Simard, M., 2017. Distribution and drivers of global mangrove forest change, 1996-2010. PLoS. One 12, e0179302. https://doi.org/10.1371/journal.pone.0179302.

Vogt, P., Riiitters, K.H., Caudullo, G., Eckhardt, B., 2019. FAO – State of the World's Forests : Forest Fragmentation. EU Science Hub.

Wang, T.T., Shao, S., Fan, S.Di., Tang, W.Q., Miao, J.W., Wang, S., Cao, X.C., Liu, C., Ying, G.G., Chen, Z.B., Zhou, H.L., Diao, X.P., Mo, L., 2024. Occurrence, distribution, and risk assessment of antibiotics in a typical aquaculture area around the Dongzhai Harbor mangrove forest on Hainan Island. Sci. Total Environ. 920, 170558. https://doi.org/10.1016/j.scitotenv.2024.170558.

Wang, W., Zhu, L., Li, L., Xue, X., Feng, Y., Xing, H., 2023. A LandTrendr algorithm-based study of forest disturbance from 2000 to 2020 in Jilin province, China. Pol. J. Env. Stud. 32, 309–319. https://doi.org/10.15244/pjoes/153969.

Wolswijk, G., Satyanarayana, B., Le, Q.D., Siau, Y.F., Ali, A.N.Bin., Saliu, I.S., Fisol, M.A.Bin., Gonnelli, C., Dahdouh-Guebas, F., 2020. Mercury concentration data from Matang Mangrove forest reserve, Malaysia. Data Br. 29, 105134. https://doi.org/10.1016/j.dib.2020.105134.

Xiong, Y., Dai, Z., Long, C., Liang, X., Lou, Y., Mei, X., Nguyen, B.A., Cheng, J., 2024. Machine learning-based examination of recent mangrove forest changes in the western Irrawaddy river Delta, southeast Asia. Catena (Amst) 234, 107601. https://doi.org/10.1016/j.catena.2023.107601.

Yang, L., Qin, G., Zhao, N., Wang, C., Song, G., 2012. Using a generalized additive model with autoregressive terms to study the effects of daily temperature on mortality. BMC. Med. Res. Methodol. 12. https://doi.org/10.1186/1471-2288-12-165.

Yaseen, M., Thapa, N., Visetnoi, S., Ali, S., Saqib, S.E., 2023. Factors determining the farmers' decision for adoption and non-adoption of oil palm cultivation in northeast Thailand. Sustain. (Switz.) 15, 1595. https://doi.org/10.3390/su15021595.

Zhu, Z., Woodcock, C.E., 2014. Continuous change detection and classification of land cover using all available Landsat data. Remote Sens. Env. 144, 152–171. https://doi.org/10.1016/j.rse.2014.01.011.

Zinnert, J.C., Nippert, J.B., Rudgers, J.A., Pennings, S.C., González, G., Alber, M., Baer, S.G., Blair, J.M., Burd, A., Collins, S.L., Craft, C., Di Iorio, D., Dodds, W.K., Groffman, P.M., Herbert, E., Hladik, C., Li, F., Litvak, M.E., Newsome, S., O'Donnell, J., Pockman, W.T., Schalles, J., Young, D.R., 2021. State changes: insights from the U.S. long term ecological research network. Ecosphere 12. https://doi.org/10.1002/ecs2.3433.